Article

Exciplex-enabled high-efficiency, fully stretchable OLEDs

https://doi.org/10.1038/s41586-025-09904-0

Received: 24 October 2024

Accepted: 12 November 2025

Published online: 14 January 2026

Check for updates

Huanyu Zhou[1,17], Hyun-Wook Kim[1,17], Shin Jung Han[1,17], Danzhen Zhang[2,3,17], Woo Jin Jeong[1], Haomiao Yu[4], Youichi Tsuchiya[5,6], Bin Hu[7], June Huh[8], Teng Zhang[2,3], Seungyeon Cho[9], Joo Sung Kim[1], Dong-Hyeok Kim[1], Hyung Joong Yun[10], Jinwoo Park[1], Kyung Yeon Jang[1], Eojin Yoon[1], Amit Kumar Harit[11], Min-Jun Sung[1], Yooseong Ahn[12], Hao Chen[1], Qingsen Zeng[1], Chan-Yul Park[1], Kwan-Nyeong Kim[1], Landep Ayuningtias[13,14], Hoichang Yang[12], Jong Chan Kim[9,15], Yun-Hi Kim[13,14], Han Young Woo[11], Chihaya Adachi[5,6], Yury Gogotsi[2,3] ✉ & Tae-Woo Lee[1,16] ✉

Fully stretchable organic light-emitting diodes (OLEDs), composed entirely of intrinsically stretchable materials, are essential for on-skin displays[1–3]. However, their low device efficiency has been a persistent barrier to practical applications for more than a decade[4]. Here we addressed this challenge by incorporating an intrinsically stretchable exciplex-assisted phosphorescent (ExciPh) layer. The elastomer-tolerant triplet-recycling mechanism mitigates exciton energy transfer limitations arising from the insulating elastomer matrix, yielding a light-emitting layer with more than 200% stretchability and an external quantum efficiency (EQE) of 21.7%. To translate this performance to fully stretchable devices, we integrated MXene-contact stretchable electrodes (MCSEs), which feature high mechanical robustness and tunable work function (WF), ensuring efficient hole and electron injection. These advances enable fully stretchable OLEDs with a record EQE of 17.0% and minimal luminescence loss under 60% strain. This approach to designing high-efficiency, mechanically compliant optoelectronics will enable the next-generation wearable and deformable displays.

Fully stretchable OLEDs are crucial for on-skin applications, such as signal visualization[4,5] (Fig. 1a). To conform to human skin, they must endure substantial stretching without performance degradation[6]. However, a notable challenge lies in the inherent trade-off between mechanical stretchability and electroluminescence efficiency[7]. Overcoming this challenge requires meticulous design that optimizes charge injection from both electrodes, as well as efficient exciton generation and use within the fully stretchable OLEDs.

Spin statistics indicate that electron and hole recombination in organic light-emitting materials generates singlet and triplet excitons in a 1:3 ratio, with singlets producing fluorescence, thereby limiting the maximum internal quantum efficiency to 25% in rigid fluorescent OLEDs[8]. For fully stretchable OLEDs, efficient charge transport and exciton energy transfer within the light-emitting materials and full use of both singlet and triplet excitons are crucial for improving electroluminescent efficiency. However, imparting stretchability to these materials often involves incorporating an insulating elastomer matrix[1] or chemical modifications with alkyl spacers[9], which greatly hinders charge transport and exciton energy transfer within the light-emitting layer owing to the presence of non-conjugated moieties. As a result, developing stretchable light-emitting materials with an EQE exceeding 20% has remained a notable challenge over the past decade. Although recent advancements, such as stretchable thermally activated delayed fluorescence (TADF) materials with alkyl spacers, have shown promise, issues with exciton generation and use continue to limit the electroluminescent performance of fully stretchable OLEDs, resulting in an EQE of 3.3% (ref. 9).

As well as modulating exciton use, achieving efficient charge injection from electrodes into the stretchable light-emitting material is vital for high electroluminescence efficiency. This process is influenced by electrical conductivity, optical transparency, electrical contact area and tunability of the WF[10]. Traditional stretchable electrodes typically use 1D metal nanowires embedded in elastomers but they have limitations as a result of their fixed WF and limited surface contact area[11]. MXenes, a family of 2D transition-metal carbides, nitrides or carbonitrides, exhibit high electrical conductivity, mechanical strength and exceptional optical transparency. These properties make MXenes highly promising for electrode materials across various applications,

[1]Department of Materials Science and Engineering, Seoul National University, Seoul, Republic of Korea. [2]A.J. Drexel Nanomaterials Institute, Drexel University, Philadelphia, PA, USA. [3]Department of Materials Science and Engineering, Drexel University, Philadelphia, PA, USA. [4]Key Laboratory of Luminescence and Optical Information, Ministry of Education, School of Physical Science and Engineering, Beijing Jiaotong University, Beijing, People's Republic of China. [5]Center for Organic Photonics and Electronics Research (OPERA), Kyushu University, Fukuoka, Japan. [6]Department of Applied Chemistry, Kyushu University, Fukuoka, Japan. [7]Department of Materials Science and Engineering, University of Tennessee, Knoxville, TN, USA. [8]Department of Chemical and Biological Engineering, Korea University, Seoul, Republic of Korea. [9]Department of Integrated Display Engineering, Yonsei University, Seoul, Republic of Korea. [10]Research Center for Materials Analysis, Korea Basic Science Institute, Daejeon, Republic of Korea. [11]Department of Chemistry, Korea University, Seoul, Republic of Korea. [12]Department of Chemical Engineering, Inha University, Incheon, Republic of Korea. [13]Department of Chemistry, Gyeongsang National University, Jinju, Republic of Korea. [14]Research Institute of Molecular Alchemy (RIMA), Gyeongsang National University, Jinju, Republic of Korea. [15]Department of Electrical and Electronic Engineering, Yonsei University, Seoul, Republic of Korea. [16]Institute of Engineering Research, Research Institute of Advanced Materials, Soft Foundry, Seoul National University, Seoul, Republic of Korea. [17]These authors contributed equally: Huanyu Zhou, Hyun-Wook Kim, Shin Jung Han, Danzhen Zhang. ✉e-mail: gogotsi@drexel.edu; twlees@snu.ac.kr

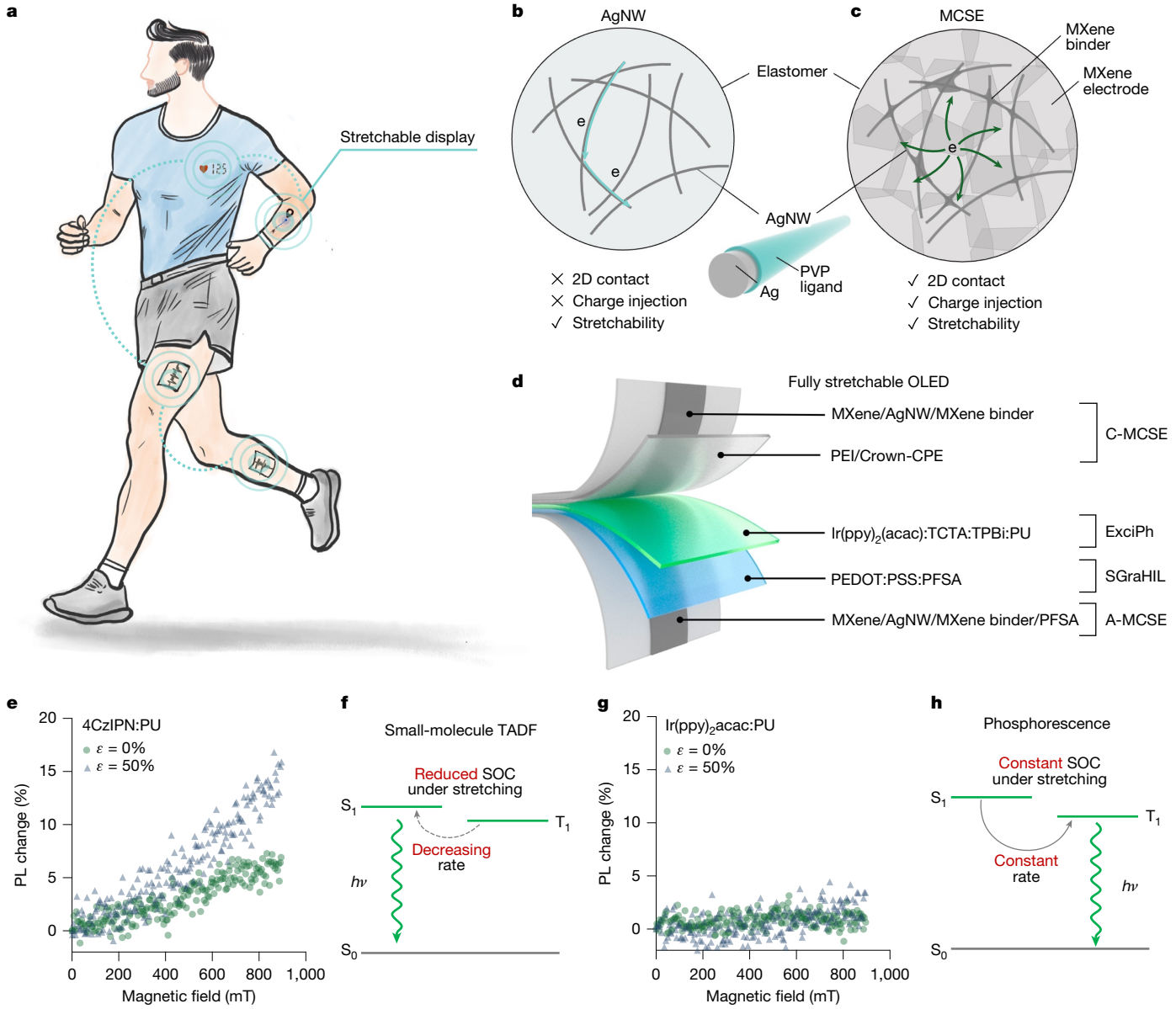

Fig. 1 | High-efficiency, fully stretchable OLEDs. a, Conceptual illustration of stretchable displays affixed to human skin for visualizing skin sensor signals. **b**,**c**, Comparison of silver nanowire (AgNW) stretchable electrodes (**b**) and MXene-contact stretchable electrodes (MCSEs) composed of AgNWs, MXene and MXene binder (**c**). PVP, polyvinylpyrrolidone. **d**, Schematic illustration of the phosphorescent fully stretchable OLEDs, composed of stretchable layers: $Ti_3C_2T_x$ MXene (in which T_x represents surface functional groups such as −OH, −O, −Cl and −F); A-MCSE (MCSE for anodes); PFSA (perfluorosulfonic acid ionomer); SGraHIL (stretchable gradient hole-injection layer); ExciPh (exciplex-assisted phosphorescence); and Crown-CPE (conjugated polyelectrolyte terminated with crown ether or anionic sulfonate groups, with tetramethylammonium as the counterion to lower the WF); C-MCSE (MCSE for cathodes). **e**, In situ magneto-PL of 4CzIPN:PU (1.5 mg ml^{-1} 4CzIPN in 2 mg ml^{-1} PU) before and after applying 50% tensile strain under 405-nm laser excitation. 4CzIPN, a commercially available small-molecule TADF material, is mixed with PU for stretchable applications. **f**, Triplet exciton harvesting process of the stretchable TADF materials under 50% strain. Dashed line, decrease in RISC rates after stretching, resulting in a reduced triplet-harvesting efficiency. S_0, ground state; S_1, singlet excited state; T_1, triplet excited state. **g**, In situ magneto-PL of $Ir(ppy)_2acac$:PU (1.5 mg ml^{-1} $Ir(ppy)_2acac$ in 2 mg ml^{-1} PU) before and after applying 50% tensile strain. $Ir(ppy)_2acac$ is a representative commercially available phosphorescent dopant. **h**, Triplet exciton harvesting process of the stretchable phosphorescence under 50% strain. Solid line, stable ISC after stretching, resulting in constant triplet-harvesting efficiency.

including energy storage and tunable electromagnetic interference shielding[12–14]. In our recent work, MXene transparent electrodes have been demonstrated to exhibit tunable WF and show great potential for use in flexible OLEDs[15,16]. Given their outstanding electrical, optical and mechanical properties, MXene-based transparent electrodes are particularly promising for use as electrodes in fully stretchable OLEDs. However, this application remains unexplored owing to the lack of a strategy to provide efficient charge injection in stretchable devices.

In this study, we addressed the long-standing challenge of low efficiency in fully stretchable OLEDs by overcoming the energy-transfer limitations posed by the insulating elastomer matrix. We introduced a stretchable ExciPh layer composed of a phosphorescent dopant, exciplex cohosts and a stretchable elastomer matrix, which enables efficient triplet harvesting by means of an elastomer-tolerant triplet-recycling mechanism. The ExciPh layer achieved stretchability exceeding 200% and OLEDs incorporating this layer and rigid electrodes achieved a high EQE of 21.7%. Furthermore, we developed MCSEs featuring a tunable WF and 2D electrical contact, ensuring efficient injection of both holes and electrons with excellent mechanical stability (Fig. 1b,c). As a result, we demonstrate fully stretchable OLEDs that achieve an unprecedented

high EQE of 17.0% while maintaining excellent mechanical compliance (Fig. 1d).

Comparison of triplet-harvesting emitters

Harvesting triplets in stretchable organic light-emitting materials necessitates using a spin-flip process to transform non-radiative triplets into radiative singlets[17]. This process is challenging in TADF materials, particularly under mechanical stretching (Extended Data Fig. 1a). Increasing the spin-flip in a reverse intersystem crossing (RISC) process involves either reducing the energy gap (ΔE_{ST}) between the lowest singlet and triplet excited states or increasing spin–orbit coupling (SOC)[18]. ΔE_{ST} is an intramolecular characteristic that can be achieved using donor–acceptor chemical structures with large dihedral angles[19]. However, SOC is sensitive to changes in intermolecular distance under stretching[20].

To quantify the relationship between SOC and mechanical stretching in TADF materials, we dispersed the TADF molecule 1,2,3,5-tetrakis(carbazol-9-yl)-4,6-dicyanobenzene (4CzIPN) into a thermoplastic polyurethane (PU) matrix to enable studies of magneto-photoluminescence (PL) under strain. Under an external magnetic field of up to 900 mT, unstretched 4CzIPN exhibited an approximately 5% increase in PL intensity, indicating that spin-mixing was not substantially affected owing to the presence of SOC in unstretched films (Fig. 1e). On mechanical stretching, the same magnetic field induced a >15% increase in PL intensity, suggesting a strain-induced reduction in SOC. This result was accompanied by the prolonged PL lifetime (Extended Data Fig. 1b), a redshift in the PL peak from 501 to 512 nm and a 10-nm broadening of the full width at half maximum (Extended Data Fig. 1c). A similar trend was observed even in the highly diluted 4CzIPN film (photoluminescence quantum yield, PLQY > 90%), in which intermolecular interactions were minimized, further supporting that the enhanced magneto-PL response under strain primarily originates from the reduced SOC under mechanical stretching (Supplementary Fig. 1a). These findings collectively suggest that tensile strain suppresses RISC by weakening SOC in TADF systems, thereby reducing the triplet exciton harvesting efficiency (Fig. 1f and Supplementary Text 1).

By contrast, phosphorescent materials such as bis(2-phenylpyridine) (acetylacetonate) iridium(III) ($Ir(ppy)_2acac$) complex exhibit intrinsically strong SOC owing to the high atomic number of iridium[21] (Extended Data Fig. 1d). When subjected to an external magnetic field of 900 mT, the PL intensity showed negligible changes (Fig. 1g). Notably, even under 50% strain, the spin-mixing rate remained unaffected, confirming that the strong SOC ensures intact intramolecular intersystem crossing (ISC) from singlet to triplet during stretching. Consequently, the PL peak remained stable at 519 nm and the PL lifetime showed negligible variation with strain (Extended Data Fig. 1e,f). These results demonstrate that the inherent strong SOC in $Ir(ppy)_2acac$ enables efficient spin-flip process under mechanical stretching and stable triplet harvesting under strain (Fig. 1h and Supplementary Fig. 1b), establishing it as an ideal dopant for fully stretchable OLEDs.

Conversion to stretchable phosphorescent materials

The stretchable ExciPh layer was developed by dispersing the $Ir(ppy)_2acac$ in a host to mitigate aggregation-induced concentration quenching (Supplementary Fig. 2a). Tris(4-carbazoyl-9-ylphenyl)amine (TCTA) and 2,2′,2″-(1,3,5-benzinetriyl)-tris(1-phenyl-1-H-benzimidazole) (TPBi) serve as exciplex cohosts, with PU as a stretchable elastomer matrix. When the ExciPh layer is excited by a light source, an exciplex forms between TCTA and TPBi and is then transferred to the dopant (Supplementary Fig. 2b). Molecular dynamics (MD) simulations estimated the binding energy between TCTA and TPBi to be 119.2 kcal mol^{-1}, facilitating efficient exciplex formation (Supplementary Fig. 3). This was confirmed by the broadening and redshift in the PL spectra of exciplex compared with the pristine spectra of TCTA and TPBi (Fig. 2a, Supplementary Fig. 2c and Supplementary Text 2). Compared with single-host systems, the ExciPh layer achieved more triplet harvesting and a higher PL intensity (Supplementary Fig. 4).

The thermoplastic PU elastomer matrix was incorporated to improve the stretchability of the ExciPh layer. PU addition diluted charge trapping on the dopant, thereby increasing both PL intensity and PL lifetime[1,22] (Supplementary Fig. 5a–c). At concentrations ≤2 mg ml^{-1}, PU had no observable effect on exciplex formation, with the PL peak consistently maintained at 450 nm (Fig. 2b). Moreover, the spin-flipping rate of the exciplex remained stable across varying PU concentrations (Supplementary Fig. 5d). This stability is attributed to the robust molecular interaction between TCTA and TPBi (Supplementary Fig. 3), preserving the spin-flipping rate of the exciplex across different PU concentrations[23].

Conversely, replacing the polar PU matrix with nonpolar elastomers resulted in pronounced aggregation and PL quenching, attributed to the marked miscibility mismatch between components (Supplementary Figs. 6–8, Extended Data Fig. 2, Supplementary Tables 1 and 2 and Supplementary Text 3). Grazing incidence X-ray diffraction of the stretchable ExciPh layer confirmed its fully amorphous nature and uniform component distribution (Supplementary Fig. 9). Notably, the ExciPh layer was uniformly coated on a 3-inch styrene-ethylene-butylene-styrene (SEBS) substrate and subjected to tensile strain and twisting, demonstrating its potential scalability for stretchable displays (Fig. 2c).

To investigate the influence of the PU elastomer matrix on photophysical processes, we compared ExciPh with single-host and exciplex-free cohost systems. In all cases without using the insulating PU, singlets and triplets can be transferred to the dopant by means of Förster resonance energy transfer (FRET) and Dexter energy transfer (DET), respectively (Supplementary Fig. 10). On introducing the PU matrix, DET is substantially suppressed owing to the presence of insulating PU between host and dopant molecules, as DET requires short-range electron exchange, leading to non-radiative triplet loss (Fig. 2d).

By contrast, the ExciPh system uses exciplex cohosts that form charge-transfer excited states with spatially separated highest occupied molecular orbital (HOMO) and lowest unoccupied molecular orbital (LUMO), enabling a small ΔE_{ST} and efficient RISC. Although DET is suppressed by the insulating PU matrix, triplet excitons undergo RISC within the exciplex cohosts to form singlet excitons, which are then transferred to the dopant through long-range FRET. This elastomer-tolerant triplet-recycling mechanism enables effective triplet harvesting even in the presence of PU (Fig. 2e).

To validate our concept, we first calculated the Förster radius (R_0) of ExciPh, exciplex-free cohost and single-host systems using experimentally measured optical properties (Supplementary Figs. 11–19, Supplementary Tables 3 and 4 and Supplementary Text 4). In all cases, R_0 slightly increased on PU incorporation, indicating that FRET remains the dominant transfer pathway in the insulating matrix (Supplementary Fig. 19). To further verify the modulation of DET and FRET by adding PU, we performed temperature-dependent measurements using a streak camera (Supplementary Figs. 20–22). The PL spectra at the 30-ns timescale revealed that energy transfer from the single host to the dopant was substantially hindered by the PU matrix (Supplementary Figs. 23–25). Although both cohost systems exhibited minimal spectral shifts after adding PU, the reduction in PL lifetimes in the exciplex-free cohosts indicated that both DET and FRET were suppressed by PU, resulting in non-radiative energy loss (Supplementary Fig. 26 and Fig. 2f,g). Conversely, in the ExciPh system, exciplex formation remains intact, allowing triplet excitons to undergo RISC and subsequently transfer to the dopant through long-range FRET, resulting in an increased PL lifetime (Fig. 2h).

To quantify the triplet-harvesting efficiency, we performed time-resolved photoluminescence (TRPL) measurements on the stretchable host materials (blended with PU) in both the presence and the

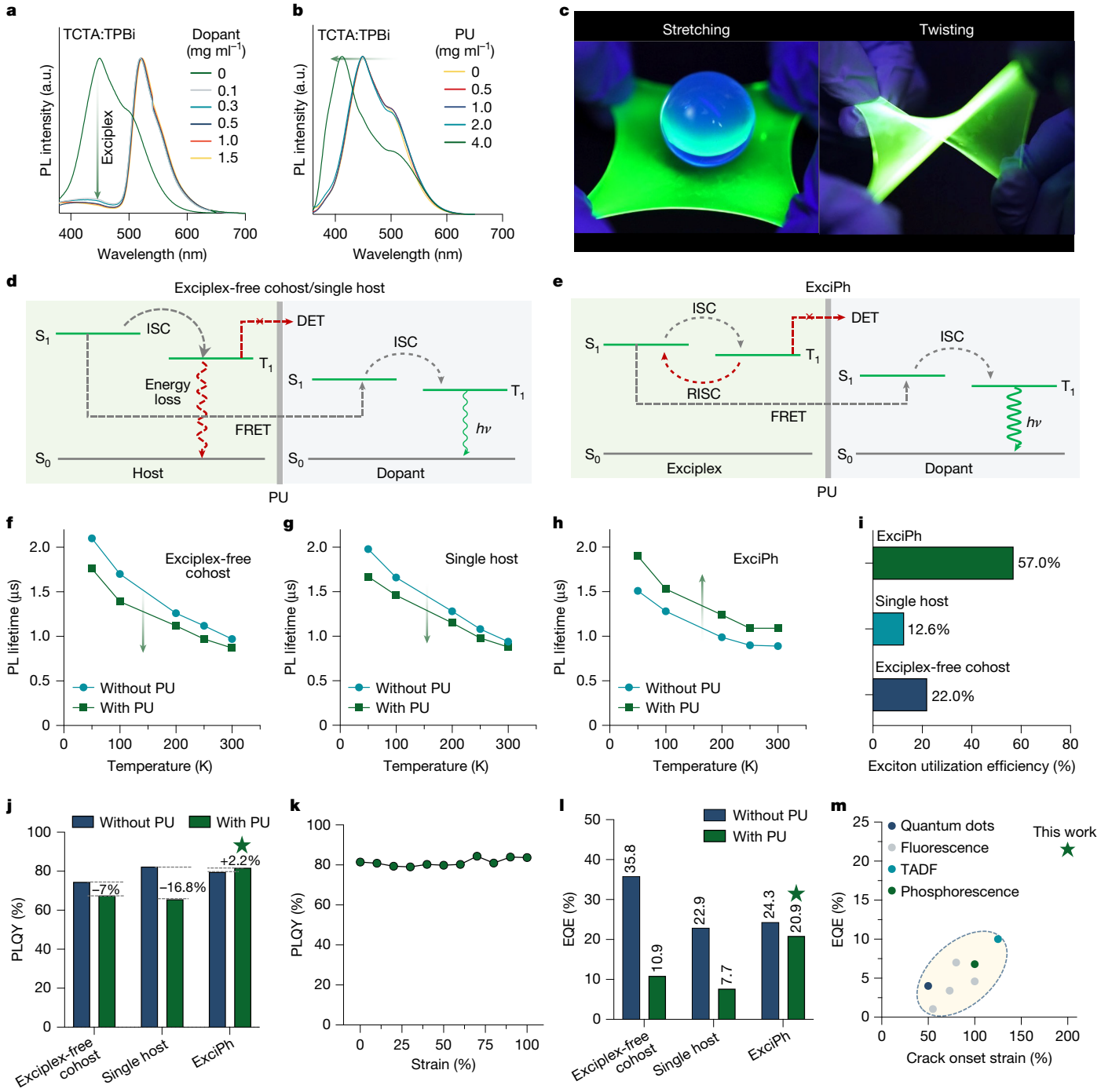

Fig. 2 | Stretchable phosphorescent layer for highly efficient, fully stretchable OLEDs. a, PL spectra of the ExciPh film with increasing concentrations of $Ir(ppy)_2acac$, ranging from 0 to 1.5 mg ml^{-1}, under an excitation wavelength of 337 nm. **b**, PL spectra of TCTA:TPBi (exciplex cohosts for ExciPh) with increasing PU loading. The film thickness is maintained at 40 nm. **c**, Photographs of the biaxially stretched (left) and twisted (right) ExciPh films deposited on a 5-cm × 5-cm stretchable substrate. **d**, Energy-level schematic of conventional exciplex-free cohost and single-host systems doped with $Ir(ppy)_2acac$. On PU incorporation, DET is suppressed by the insulating matrix, leading to non-radiative triplet loss. **e**, Energy-level schematic of the ExciPh system. Despite DET suppression owing to the PU incorporation, triplet excitons undergo RISC in the exciplex cohosts, followed by FRET to the phosphorescent dopant, enabling elastomer-tolerant triplet recycling and efficient triplet harvesting. **f**–**h**, Temperature-dependent PL lifetime before and after PU addition for exciplex-free cohost (**f**), single-host (**g**) and ExciPh (**h**) systems, extracted from streak-camera measurements. **i**, Exciton utilization efficiency of exciplex-free cohost, single-host and ExciPh systems with the addition of PU. **j**, PLQY measurement of exciplex-free cohost, single-host and ExciPh systems before and after adding PU. **k**, PLQY measurement of the ExciPh with varying tensile strain. PLQY was calculated using several direct and indirect light-emission measurements under different strains. **l**, EQE of devices with exciplex-free cohost, single-host and ExciPh systems with and without PU in ITO-based rigid devices. **m**, Comparison of EQE and crack onset strain in rigid OLEDs that use stretchable light-emitting materials. EQE measured in rigid state; 200% denotes crack onset strain of the emissive layer. a.u., arbitrary units.

absence of the phosphorescent dopant (Supplementary Fig. 27). Exciton utilization efficiency in the ExciPh system was determined to be 57.0%, substantially surpassing that of the single host (12.6%) and the exciplex-free cohosts (22.0%), indicating the effectiveness of exciplex-assisted energy transfer even with the presence of an insulating elastomer matrix (Fig. 2i and Supplementary Text 5). Correspondingly, after incorporation of PU, the PLQY of ExciPh increased by 2.2%, whereas exciplex-free cohost and single-host systems showed a reduction of 7% and 16.8%, respectively (Fig. 2j). Notably, the stretchable ExciPh layer remained at approximately 80% PLQY under 100% tensile strain (Fig. 2k), with negligible changes in donor–acceptor distance, thereby preserving its intact triplet-harvesting efficiency (Extended Data Fig. 3 and Supplementary Text 6). MD simulations further corroborated the structural robustness of the stretchable ExciPh layer, revealing no observable changes in the intermolecular distance between host and dopant under strain (Supplementary Figs. 28 and 29).

Mechanically, the stretchable ExciPh layer exhibited excellent robustness, sustaining strains up to 200% without crack formation (Extended Data Fig. 4). Under stretching, the ExciPh demonstrated clear elongation of PU polymer chains along the stretching direction, with its amorphous nature effectively preventing crack formation (Supplementary Fig. 30). Increasing the PU concentration from 2 to 4 mg ml^{-1} decreased the stretchable ExciPh's Young's modulus from 237.8 to 157.6 MPa (Supplementary Fig. 31). These mechanical properties were also validated using the buckling-method measurements (Supplementary Fig. 32).

Electroluminescent properties were subsequently evaluated in rigid OLEDs to establish the maximum achievable efficiency. Devices incorporating ExciPh without PU had an EQE of 24.3% and a current efficiency of 74.5 cd A^{-1} (Extended Data Fig. 5). On incorporating the stretchable ExciPh layer, the device retained a high EQE of 21.7% and current efficiency of 66.1 cd A^{-1} at 35 cd m^{-2}, indicating minimal efficiency loss. By contrast, devices based on single-host or exciplex-free cohost systems exhibited notable efficiency decrease on conversion to stretchable formats, owing to inefficient triplet harvesting (Fig. 2l and Extended Data Figs. 5–7). These results proved the high triplet-harvesting efficiency of elastomer-tolerant triplet recycling, demonstrating simultaneous enhancement of both stretchability and luminescence efficiency compared with previously reported stretchable light-emitting materials (Fig. 2m, Supplementary Figs. 33 and 34 and Supplementary Table 5).

To evaluate the electroluminescent characteristics of the ExciPh under stretching, films of varying thicknesses were transferred onto polydimethylsiloxane (PDMS) stamps and laminated onto rigid substrates (Supplementary Fig. 35). Thick ExciPh (>50 nm) initially hindered charge injection but exhibited an enhanced EQE under strain owing to thickness reduction (Supplementary Fig. 36). At 100% strain, the EQE of a 50-nm-thick ExciPh device decreased by only 10.8% (Supplementary Fig. 37), in contrast to a 57.5% decrease observed for the single-host device at 50% strain (Supplementary Fig. 38). The stretchable ExciPh layer exhibited exceptional mechanical robustness with only an 18.6% decrease in EQE after 1,000 cycles at 40% strain (Supplementary Fig. 39). Time-resolved electroluminescence measurements revealed that the initial decay time of 84.6 μs before strain, associated with exciplex-mediated energy transfer[24], increased to 172.9 μs at 50% strain, accompanied by overshoot features indicative of enhanced trap-assisted recombination[25] (Supplementary Fig. 40). Furthermore, the recombination zone shifted towards the electron injection interface under strain, suggesting the formation of strain-activated trap states (Extended Data Fig. 8).

MCSEs for fully stretchable OLEDs

Efficient charge injection into the stretchable ExciPh layer requires transparent electrodes with WF tunability, 2D electrical contact, high conductivity and stretchability. To meet these requirements, we developed MCSEs composed of a 2D MXene interlayer on top of stretchable electrodes that use silver nanowires (AgNWs) (Fig. 3a). As demonstrated by the characteristic peaks of MCSEs in the Raman spectra, the 2D MXene interlayer was successfully transferred to the SEBS stretchable substrate (Supplementary Fig. 41a).

MXenes are susceptible to moisture owing to the rapid intercalation of hydrated lithium ions during synthesis (≈0.38 nm)[26], so the post-fabrication heating temperature was >100 °C to ensure the removal of water intercalation. This process compacted the layered structure of MXene films[27]. In X-ray diffraction patterns, the MCSE has a characteristic (002) peak at 7.96°, corresponding to a channel width of about 0.11 nm, smaller than the hydrated lithium ions (Supplementary Fig. 41b). Consequently, post-fabrication heating greatly enhances the processability of the MCSE in aqueous solution without altering its resistance (Supplementary Fig. 42).

To reduce the junction resistance and enhance the electrical conductivity of percolation networks, diluted MXene was used as a conductive binder to connect ('weld') AgNW/AgNW and AgNW/MXene interfaces (Fig. 3b). This approach substantially enhances the carrier mobility from 1.4 to 85.9 $cm^2 V^{-1} s^{-1}$ of the MCSE, which is slightly higher than the pristine MXene mobility of 73.4 $cm^2 V^{-1} s^{-1}$ (Fig. 3c). Furthermore, temperature-dependent resistance measurements revealed that, although hopping transport dominated in AgNW percolation networks, the MCSEs overcame this limitation, as evidenced by higher conductivity in the low-temperature region (Fig. 3d). The introduction of MXene enhances long-range connection between AgNW/MXene percolation networks, increasing the conductivity and charge-spreading capability of the MCSE (Supplementary Text 7). The resulting MCSE demonstrated a sheet resistance of 30 Ω sq^{-1} and a transmittance >85% at 550 nm (Supplementary Fig. 43). Even after surface modifications, the WF of the MCSEs was widely tunable from 3.79 to 5.71 eV without compromising their electrical and optical properties (Fig. 3e).

The mechanical stretchability of MCSEs was evaluated under static and cyclic tensile strain. Under 40% tensile strain, the resistance change ($\Delta R/R_0$) was much lower in MCSEs (0.98) than in AgNW electrodes (5.53) (Extended Data Fig. 9a). Furthermore, during 500 cycles of 40% cyclic strain, $\Delta R/R_0$ was consistently lower in the MCSE than in AgNW, that is, the MCSE has better electrical stability than AgNW under strain (Extended Data Fig. 9b). No noticeable protrusions or slippage were observed during cyclic stretching (Supplementary Fig. 44), attributed to favourable interactions between AgNW ligands and the SEBS elastomer matrix[11].

Furthermore, Fourier-transform infrared and X-ray photoelectron spectroscopy analyses revealed the presence of hydrogen-bonding interactions between AgNW ligands and MXene (Supplementary Figs. 45 and 46). These interactions were further confirmed using in situ ultraviolet–visible (UV–Vis) spectroscopy. On applying a reverse voltage sweep from 0.2 V, the plasmon peak of MXene shifted from 815 to 766 nm at −0.4 V and further to 727 nm at −0.6 V, indicating progressive hydroxyl deprotonation. By contrast, the MCSE exhibited a smaller but more rapid shift to 748 nm (Fig. 3f). Given the WF difference—4.20 eV for AgNW[11] and 4.89 eV for MXene[15]—a spontaneous charge transfer from AgNW to MXene occurs, which potentially accelerates deprotonation. However, hydrogen-bonding interactions between AgNW ligands and MXene partially suppress deprotonation, resulting in a less pronounced peak shift compared with pristine MXene (Fig. 3g). Therefore, the superior mechanical and morphological stability of MCSE is attributed to hydrogen-bonding interactions between AgNW ligands and MXene (Fig. 3h and Extended Data Fig. 9c). Compared with other reported stretchable electrodes, our MCSE excels in electrical, mechanical and optical properties (Supplementary Table 6 and Supplementary Text 8).

To further enhance charge injection from the MCSE to the stretchable ExciPh layer, we developed a stretchable gradient hole injection layer (SGraHIL) by incorporating perfluorosulfonic acid ionomer (PFSA)

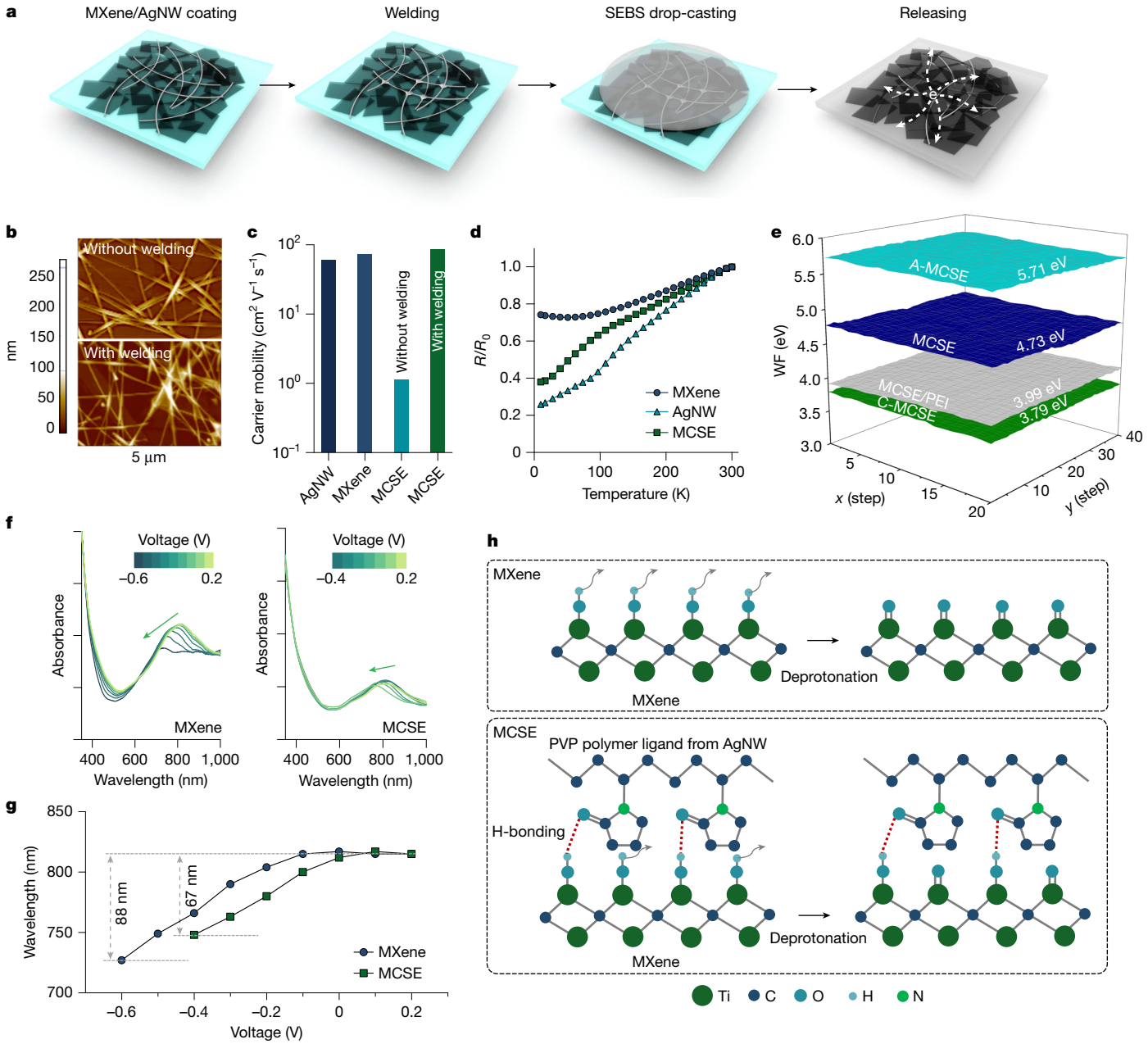

Fig. 3 | MCSEs for highly efficient, fully stretchable OLEDs. a, Schematic of the MCSE embedding process. MXene and AgNWs were sequentially deposited, followed by welding the AgNWs and MXene junctions using a MXene binder (MXene aqueous solution at 0.5 mg ml^{-1}). SEBS elastomer is then drop-cast over the substrate. After this process, the layer of conductive materials embedded in the elastomer was released from the glass substrate to yield the MCSE. **b**, Atomic force microscopy topography images of AgNW before and after welding using 0.5 mg ml^{-1} MXene solution to weld the junctions of AgNWs. **c**, Carrier mobility of electrodes: MXene and AgNW tested as rigid electrodes on glass substrates and MCSEs with and without MXene welding. **d**, Temperature-dependent resistance change of AgNW, MXene and the MCSE. Resistance values are normalized to their respective initial values at 300 K. **e**, Kelvin probe WF mapping of pristine MCSE, MCSE with PEI surface modifier (MCSE/PEI), anodes surface-modified using PFSA (A-MCSE) and cathodes surface-modified using PEI and Crown-CPE (C-MCSE). Each step in the *x*-axis and *y*-axis represents 635 nm. **f**, In situ UV–Vis absorption spectra of MXene (left) and the MCSE (right) in 1 M H_2SO_4 were obtained using a specially designed three-electrode cell that enables simultaneous electrochemical reactions and absorption spectra recording. **g**, Evolution of absorption peaks for MXene and the MCSE at various voltages; data extracted from **f**. **h**, Schematic illustration of electrochemical reaction mechanisms for MXene and the MCSE in acidic environments. In the anodic process, deprotonation dominates the reaction in MXene.

and a nonionic surfactant into poly(3,4-ethylenedioxythiophene):poly(styrenesulfonate) (PEDOT:PSS). This design establishes a vertical WF gradient, suppresses exciton quenching and imparts excellent mechanical stretchability (Extended Data Fig. 10, Supplementary Figs. 47–50 and Supplementary Text 9).

Notably, SGraHIL, ExciPh and adjacent interfacial layers showed no discernible phase separation or morphological degradation after two weeks of storage or mechanical deformation, suggesting minimal interdiffusion between small-molecule and polymeric components and confirming the structural stability of the multilayer system (Supplementary Figs. 51–55 and Supplementary Text 10).

Demonstration of fully stretchable OLEDs

Using all of the developed components, we fabricated fully stretchable OLEDs composed entirely of stretchable elements, including

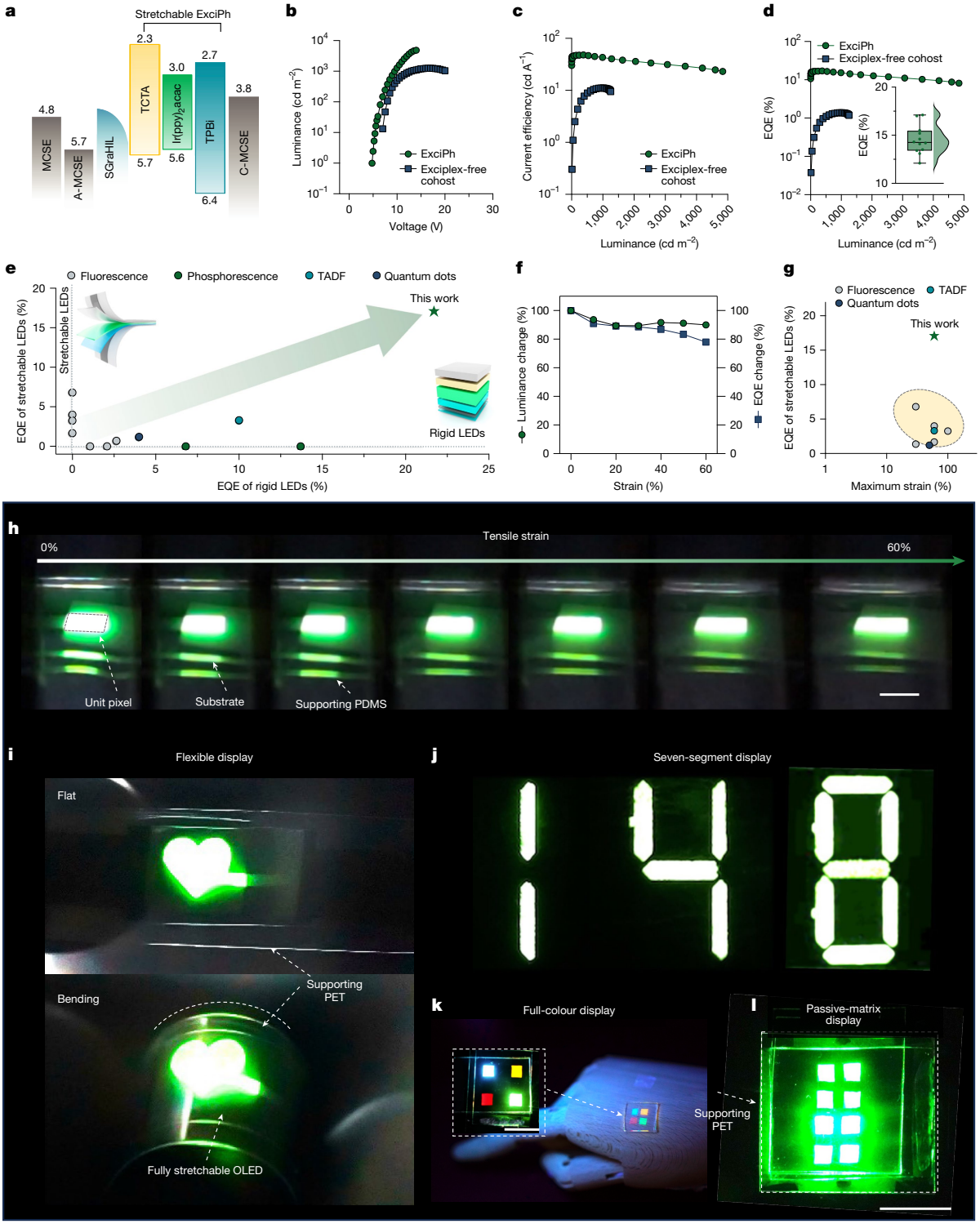

Fig. 4 | Demonstration of highly efficient, fully stretchable OLEDs. a, Energy-level alignment of the fully stretchable OLEDs. **b**–**d**, Luminance–voltage, current efficiency–luminance and EQE–luminance characteristics of fully stretchable OLEDs using ExciPh and exciplex-free cohosts. Inset in **d** shows a histogram of peak EQE values across >10 devices. **e**, Comparison of the EQE of previously reported fully stretchable OLEDs and rigid LEDs using a stretchable light-emitting layer. The circles on the horizontal dashed line represent the EQE of rigid LEDs using the stretchable light-emitting layer without applying it to fully stretchable devices. The circles on the vertical dashed line stand for the EQE of fully stretchable OLEDs without applying stretchable light-emitting layers to rigid devices (details in Supplementary Fig. 57). **f**, Change in luminance and EQE of fully stretchable OLEDs versus strain at 10 V. **g**, Comparison of maximum strain versus EQE of fully stretchable OLEDs (details in Supplementary Fig. 59). **h**, Inclined top photographs of the fully stretchable OLEDs on a supporting PDMS substrate with increasing tensile strain up to 60%. The light emission from the substrate and the PDMS support represents the light trapped within the substrates and escaping from the side. Scale bar, 3 mm. **i**, Digital photograph of a heart-shaped stretchable OLED on a supporting polyethylene terephthalate (PET) substrate before and after bending. **j**, Digital photographs of a seven-segment display (details in Supplementary Fig. 60). **k**, Digital photographs of full-colour, fully stretchable ExciPh in four different colours under UV irradiation. The inset represents the photographs of full-colour, fully stretchable OLEDs under a voltage of 10 V. Scale bar, 1 cm. **l**, Digital photographs of stretchable passive-matrix OLEDs. Scale bar, 1 cm.

electrodes, light-emitting layers and functional layers (Fig. 4a and Supplementary Fig. 56). It featured a low turn-on <5.0 V and a peak luminance of 4,840 cd m^{-2} (Fig. 4b). Notably, our device had a maximum EQE of 17.0% and a current efficiency of 47.9 cd A^{-1} at 376 cd m^{-2} (Fig. 4c,d). By comparison, the device with exciplex-free cohosts only had an EQE of 1.4% (Fig. 4d). The more than tenfold higher EQE using ExciPh highlights the efficient exciplex energy transfer over the insulating PU matrix, substantially enhancing light emission. Both rigid OLEDs using the stretchable ExciPh and the fully stretchable OLED achieved record efficiencies, outperforming various types of LED using different stretchable emitting layers, including fluorescence, phosphorescence, TADF and quantum dots, as well as their corresponding fully stretchable configurations (Fig. 4e, Supplementary Fig. 57 and Supplementary Table 7). Static stretching tests conducted in a nitrogen-filled glovebox confirmed the mechanical robustness of the device, with only a 10.6% decrease in luminance and a 22.0% drop in EQE at 60% strain (Fig. 4f). Under 20% cyclic strain, the device retained more than 83% of its initial efficiency after 100 cycles, with further degradation attributed primarily to interfacial instability rather than the ExciPh emissive layer (Supplementary Fig. 58). This mechanical resilience compares favourably to previously reported fully stretchable OLEDs (Fig. 4g,h and Supplementary Fig. 59). The fully stretchable OLED with a heart-shaped patterned MCSE was also durable under flexible applications (Fig. 4i). Furthermore, the device was successfully integrated into a seven-segment display, which showed the numbers '1', 4' and '8' (Fig. 4j and Supplementary Fig. 60).

To further demonstrate the wide applicability of our fully stretchable OLED, we achieved a monolithic full-colour fully stretchable display incorporating four different dopants in the stretchable ExciPh: tris(1-phenylisoquinoline)iridium(III) ($Ir(piq)_3$) for red, $Ir(ppy)_2acac$ for green, bis[2-(4,6-difluorophenyl)pyridinato-C2,N](picolinato) iridium(III) (FIrPic) for blue and bis(2-phenylbenzothiazolato)(acetylacetonate)iridium(III) ($Ir(bt)_2acac$) for orange (Fig. 4k). Moreover, we demonstrated fully stretchable passive-matrix OLEDs, exhibiting their processability and potential applications of our systems in wearable electronics (Fig. 4l).

Conclusions

We address the long-standing efficiency limitation of fully stretchable OLEDs by combining delicately designed stretchable phosphorescent light-emitting material, ExciPh, with MCSEs. The strong spin–orbit coupling in ExciPh enables efficient and stable triplet exciton harvesting under strain. At the same time, the exciplex cohosts facilitate reverse intersystem crossing, thereby bypassing non-radiative losses associated with hindered Dexter energy transfer in the insulating PU matrix. The exciton utilization efficiency in the ExciPh system was determined to be 57.0%, substantially surpassing that of the single-host (12.6%) and the exciplex-free cohost (22.0%) systems, demonstrating the effectiveness of the elastomer-tolerant triplet-recycling mechanism. The ExciPh layer achieved more than 200% stretchability and a high EQE of 21.7% in devices with rigid electrodes. Meanwhile, MCSEs offer tunable work functions and robust charge injection without compromising mechanical compliance. Together, these features enabled fully stretchable OLEDs with an unprecedented high external quantum efficiency of 17.0%, maintaining stable light emission even under 60% strain. Our method substantially reduces the efficiency gap between rigid and fully stretchable OLEDs, providing a promising pathway for highly efficient stretchable optoelectronic devices.

Online content

Any methods, additional references, Nature Portfolio reporting summaries, source data, extended data, supplementary information, acknowledgements, peer review information; details of author contributions and competing interests; and statements of data and code availability are available at https://doi.org/10.1038/s41586-025-09904-0.

1. Zhang, Z. et al. High-brightness all-polymer stretchable LED with charge-trapping dilution. *Nature* **603**, 624–630 (2022).
2. Liang, J., Li, L., Niu, X., Yu, Z. & Pei, Q. Elastomeric polymer light-emitting devices and displays. *Nat. Photon.* **7**, 817–824 (2013).
3. Matsuhisa, N. et al. High-frequency and intrinsically stretchable polymer diodes. *Nature* **600**, 246–252 (2021).
4. Zhou, H., Kim, H.-W., Jeong, W. J. & Lee, T.-W. Toward intrinsically stretchable OLEDs with high efficiency. *Adv. Mater.* **37**, 2420008 (2025).
5. Shi, X. et al. Large-area display textiles integrated with functional systems. *Nature* **591**, 240–245 (2021).
6. Kim, J.-H. & Park, J.-W. Intrinsically stretchable organic light-emitting diodes. *Sci. Adv.* **7**, eabd9715 (2021).
7. Zhou, H., Kim, K.-N., Sung, M.-J., Han, S. J. & Lee, T.-W. Intrinsically stretchable low-dimensional conductors for wearable organic light-emitting diodes. *Device* **1**, 100060 (2023).
8. Adachi, C., Baldo, M. A., Thompson, M. E. & Forrest, S. R. Nearly 100% internal phosphorescence efficiency in an organic light-emitting device. *J. Appl. Phys.* **90**, 5048–5051 (2001).
9. Liu, W. et al. High-efficiency stretchable light-emitting polymers from thermally activated delayed fluorescence. *Nat. Mater.* **22**, 737–745 (2023).
10. Han, T.-H. et al. Extremely efficient flexible organic light-emitting diodes with modified graphene anode. *Nat. Photon.* **6**, 105–110 (2012).
11. Zhou, H. et al. Graphene-based intrinsically stretchable 2D-contact electrodes for highly efficient organic light-emitting diodes. *Adv. Mater.* **34**, 2203040 (2022).
12. VahidMohammadi, A., Rosen, J. & Gogotsi, Y. The world of two-dimensional carbides and nitrides (MXenes). *Science* **372**, eabf1581 (2021).
13. Li, X. et al. MXene chemistry, electrochemistry and energy storage applications. *Nat. Rev. Chem.* **6**, 389–404 (2022).
14. Han, M. et al. Electrochemically modulated interaction of MXenes with microwaves. *Nat. Nanotechnol.* **18**, 373–379 (2023).
15. Zhou, H. et al. Overcoming the limitations of MXene electrodes for solution-processed optoelectronic devices. *Adv. Mater.* **34**, 2206377 (2022).
16. Ahn, S. et al. A 2D titanium carbide MXene flexible electrode for high-efficiency light-emitting diodes. *Adv. Mater.* **32**, 2000919 (2020).
17. Cui, L.-S. et al. Fast spin-flip enables efficient and stable organic electroluminescence from charge-transfer states. *Nat. Photon.* **14**, 636–642 (2020).
18. Uoyama, H., Goushi, K., Shizu, K., Nomura, H. & Adachi, C. Highly efficient organic light-emitting diodes from delayed fluorescence. *Nature* **492**, 234–238 (2012).
19. Yang, Z. et al. Recent advances in organic thermally activated delayed fluorescence materials. *Chem. Soc. Rev.* **46**, 915–1016 (2017).
20. Hu, B., Yan, L. & Shao, M. Magnetic-field effects in organic semiconducting materials and devices. *Adv. Mater.* **21**, 1500–1516 (2009).
21. Du, C., Wang, H., Yang, F. & Hammel, P. C. Systematic variation of spin-orbit coupling with *d*-orbital filling: large inverse spin Hall effect in 3*d* transition metals. *Phys. Rev. B* **90**, 140407 (2014).
22. Park, Y.-S. et al. Exciplex-forming co-host for organic light-emitting diodes with ultimate efficiency. *Adv. Funct. Mater.* **23**, 4914–4920 (2013).
23. Park, J. W., Cho, K. H. & Rhee, Y. M. Mechanism of Ir(ppy)3 guest exciton formation with the exciplex-forming TCTA:TPBI cohost within a phosphorescent organic light-emitting diode environment. *Int. J. Mol. Sci.* **23**, 5940 (2022).
24. Lee, J.-H., Lee, S., Yoo, S.-J., Kim, K.-H. & Kim, J.-J. Langevin and trap-assisted recombination in phosphorescent organic light emitting diodes. *Adv. Funct. Mater.* **24**, 4681–4688 (2014).
25. Weichsel, C. et al. Storage of charge carriers on emitter molecules in organic light-emitting diodes. *Phys. Rev. B* **86**, 075204 (2012).
26. Lao, J. et al. Aqueous stable Ti_3C_2 MXene membrane with fast and photoswitchable nanofluidic transport. *ACS Nano* **12**, 12464–12471 (2018).
27. Iqbal, A. et al. Anomalous absorption of electromagnetic waves by 2D transition metal carbonitride Ti_3CNT_x (MXene). *Science* **369**, 446–450 (2020).

Methods

MXene synthesis

Details of MXene synthesis and characterization are described in our previous work[15].

Crown-CPE synthesis

Details of Crown-CPE synthesis and characterization are described in our previous work[11].

Preparation of the MCSE

The preparation of the MCSE used a systematic approach. Initially, a glass substrate, measuring 2.5 cm × 2.5 cm, was rigorously cleaned by sequential sonication in acetone and isopropyl alcohol (IPA), followed by drying using a nitrogen (N_2) gun. The preparation of the MXene solution entailed diluting it to a concentration of 4 mg ml^{-1} with deionized water (DIW). To remove large aggregates, the solution was centrifuged at 2,000 rpm for 5 min. Concurrently, the cleaned glass substrate was treated with UV ozone for >10 min at approximately 19.8 mW cm^{-2} to increase its wettability, which is a critical factor for the subsequent deposition of the MXene solution.

The MXene solution was dropped onto the substrate, then allowed to rest for 2 min to enable self-assembly and then spin-coated over the whole substrate. This process was executed in two stages: the first at 2,000 rpm for 60 s to ensure uniform MXene electrode coating and the second at 6,000 rpm for 90 s to remove residual moisture. Given the propensity of moisture to penetrate the interlayers of MXene by solvation, high-speed rotation aids in narrowing these interlayers and improving solution processability. To further compact these interlayers and thereby prevent intrusion of H_2O molecules, the electrode was thermally annealed at 150 °C for 2 h in a N_2-filled environment (O_2 and H_2O, each <1 ppm) to remove surface functional groups and any intercalated moisture without causing oxidation[27].

Subsequently, we prepared a suspension of AgNWs at 2.5 mg ml^{-1} in IPA and then dropped onto the MXene electrode and spin-coated at 2,000 rpm for 60 s. These steps were repeated twice to achieve uniform coverage. The coated substrate was then heated to 120 °C for 10 min on a hotplate in ambient air to facilitate interactions at AgNW/AgNW and AgNW/MXene interfaces. To further enhance these interfaces, a diluted MXene binder solution (0.5 mg ml^{-1}) was applied using a similar spin-coating technique at 2,000 rpm for 60 s.

Before the embedding process, the as-prepared electrode was meticulously patterned using a cotton swab. Then 0.4 ml of a 180 mg ml^{-1} solution of SEBS (Asahi Kasei H1062) in toluene was drop-cast onto the prepatterned MXene/AgNWs glass substrate to ensure complete coverage. After sufficient time for the residual solvent evaporation, the electrode was readily detached from the glass substrate by water immersion.

To fabricate the MCSE for the anode (A-MCSE) with a high WF, a diluted solution of PFSA (2 wt% in IPA) was spin-coated onto the pre-prepared MCSE and then thermally annealed at 100 °C for 5 min. Conversely, for the preparation of the MCSE for the cathode (C-MCSE) with a low WF, solutions of polyethyleneimine (PEI, Sigma) and Crown-CPE were prepared in advance of the spin-coating process. PEI was dissolved in 2-methoxyethanol to achieve a concentration of 0.5 wt.% and Crown-CPE was dissolved in the same solvent at a concentration of 1.5 mg ml^{-1}. Both solutions were stirred in a N_2-filled glovebox overnight to ensure complete mixing. Subsequently, the PEI solution was spin-coated onto the MCSE at 3,000 rpm for 60 s and then the complex was heat-treated at 90 °C for 5 min. A similar process was performed using the Crown-CPE solution.

Fabrication of highly efficient, fully stretchable OLEDs

To fabricate the conventional stretchable hole injection layer (SHIL), a solution was prepared by mixing 5 wt% Triton X-100 with PEDOT:PSS (Clevios P VP AI 4083). This mixture was further diluted with IPA in a 1:1 weight-to-weight ratio to improve its wettability on the MCSE surface. By contrast, the SGraHIL was formulated by adding 1 wt% Triton X-100 to PEDOT:PSS AI 4083 and incorporating PFSA in a 1:1.5 weight ratio. Both solutions were mixed on a roller for 1 h before being used in device fabrication.

The stretchable ExciPh layer required a thermoplastic PU (Tecoflex SG-80A) solution, prepared by dissolving PU in a solvent composed of cyclohexanone and tetrahydrofuran (THF) in a 10:1 volume-to-volume ratio. This cosolvent approach was used to avoid the possibility that high THF concentrations could damage the underlying substrate. The PU solution was stirred under a N_2 atmosphere in a glovebox for >1 h. In the same glovebox, 0.9 mg of $Ir(ppy)_2acac$, 5 mg of TCTA and 5 mg of TPBi were dissolved in 1 ml of the PU solution to reduce oxygen quenching of the phosphorescent dopant's triplet state. This solution was typically prepared 12 h in advance.

To evaluate the effect of exciplex formation, we also compared the performance of the stretchable phosphorescent layer without exciplex formation. In this material, the electron transport host TPBi was replaced with diphenylbis(3-(pyridine-2-yl)phenyl)silane (2PTPS). All other experimental procedures were kept consistent with those used for the ExciPh layer, ensuring a direct comparison.

For the fully stretchable OLED fabrication, the SGraHIL solution was first filtered through a 0.45-µm syringe polyvinylidene fluoride (PVDF) filter and then spin-coated onto the A-MCSE at 4,000 rpm for 60 s. The film was annealed at 100 °C for 30 min in ambient air to form a dense and compact film, which resists attack by THF solvent. The measured thickness of the SGraHIL film was roughly 82 nm.

Following SGraHIL deposition, the substrate was transferred into a N_2 environment in a glovebox. The stretchable ExciPh solution was filtered through a 0.45-µm syringe PVDF filter first and then spin-coated on the SGraHIL at 3,000 rpm for 60 s. The resultant film was then heat-treated at 90 °C for 5 min. The resulting film thickness was about 50 nm. Then, to establish an electrical interface between the stretchable ExciPh and the C-MCSE, the C-MCSE was gently placed onto the stretchable ExciPh layer and pressed with tweezers to expel any trapped air bubbles. The laminated structure was then annealed at 50 °C for 15 min to guarantee a robust electrical contact. Finally, to protect the fully stretchable OLED from oxygen and moisture, it was placed in a N_2 atmosphere in a glovebox.

Patterning of MCSEs for the seven-segment display

To create the MCSE with the desired pattern, a photolithography method was used to deposit the MCSE precisely on specific areas. First, a positive photoresist (AZ GXR-601) was deposited on the glass substrate by spin-coating at 4,000 rpm for 60 s, to yield a 1-µm-thick photoresist layer. Then the photoresist was soft-baked at 120 °C for 5 min to remove solvent and strengthen the adhesion between the photoresist and the glass substrate. To define the pattern, the substrate was irradiated using UV to initiate the formation of the bank structure for the subsequent patterning process. Immediately following this step, the substrate was immersed in a developer solution (AZ 300 MIF) for 30 s and then thoroughly rinsed with DIW to eliminate any excess developer. The specimens were then hard-baked at 120 °C for 5 min to ensure full crosslinking of the photoresist. The deposition process of MXene, AgNWs and MXene binder followed the same procedure. After the welding step involving the MXene binder, the substrate was immersed in acetone for 30 s to remove the photoresist. Both MXene and AgNWs showed resistance against attack by acetone. The MCSE was embedded and released as described.

Highly efficient OLEDs using ExciPh on the rigid ITO substrate

To prepare the indium tin oxide (ITO) glass substrate with a thickness of 70 nm and windmill pattern for device integration, a systematic cleaning procedure was used. Initially, the substrate was thoroughly

rinsed using acetone and IPA and then dried using a N_2 gun to ensure the removal of any surface contaminants. The clean ITO glass was then subjected to UV ozone treatment for 10 min at approximately 19.8 mW cm^{-2} to increase its wettability, which is crucial for the subsequent application of the SGraHIL.

The preparation of the SGraHIL solution and its spin-coating onto the ITO glass used the same methods as those for the fully stretchable OLED fabrication. After applying the SGraHIL, the specimen was coated with stretchable ExciPh and then the substrate was transferred to a high-vacuum thermal evaporator chamber, maintained at a pressure less than 10^{-7} torr. In this chamber, a sequential deposition was carried out, starting with 45 nm of TPBi, followed by 2 nm of LiF and, finally, 100 nm of Al. A shadow mask was used during the deposition to define the device pixels precisely.

In the final step, the device was encapsulated using UV-curable epoxy resin to seal it with a glass lid. The encapsulation process was completed by curing under 365-nm UV light for 15 min to ensure the development of a protective seal against environmental factors.

To isolate the impact of exciplex formation on device performance, we compared the stretchable phosphorescent layer using exciplex-free cohost and single-host systems. In the exciplex-free cohosts, the electron-transporting TPBi was substituted with 2PTPS, whereas all other fabrication conditions were identical to those used for the ExciPh system. Similarly, for the single-host device, 4,4′-bis(n-carbazolyl)-1,1′-biphenyl (CBP) was used at a concentration of 10 mg ml^{-1}, with all remaining experimental parameters held constant to enable a direct comparison.

Highly efficient OLEDs using transferred stretchable ExciPh

The ITO electrode was prepared and the SGraHIL was deposited. Transfer of stretchable ExciPh onto the SGraHIL required the use of a SiO_2 wafer that had been coated with an octadecyltrimethoxysilane (OTMS) self-assembled monolayer. For this purpose, a 100-nm-thick SiO_2 substrate was first subjected to UV ozone for 20 min to achieve a hydrophilic surface. Then a 3-mM OTMS solution in trichloroethylene was spin-coated onto the wafer. The wafer was then placed in a vacuum desiccator with 4 ml of ammonium hydroxide solution for >6 h. The wafer was cleaned by wiping with cotton swabs soaked in toluene to remove surface residues and then dried using a N_2 gun and finally cut to the desired size.

For stretchable ExciPh transfer, all procedures were conducted in a N_2-filled glovebox. First, an ultrathin layer of PU was applied to the OTMS-treated wafer. The coated wafer was dried at 120 °C for 5 min, spin-coated with stretchable ExciPh at 3,000 rpm for 60 s and then annealed at 90 °C for 5 min. A PDMS stamp, with a monomer-to-curing agent ratio of 15:1 by weight and a thickness of about 2 mm, was then pressed onto the stretchable ExciPh, with care taken to avoid bubble formation. The stretchable ExciPh was transferred to the SGraHIL surface by releasing the bilayer from the OTMS. Tensile stress was applied to the stretchable ExciPh by stretching the PDMS stamp to the desired strain and contacting it with the SGraHIL. To strengthen electrical contact and adhesion at the interface, the specimen was heat-treated at 80 °C for 3 min. The deposition conditions for TPBi, LiF and Al were the same as those used to fabricate by spin-coating.

Using this transfer-printing technique, we analysed charge-carrier recombination using bilayer-structured stretchable ExciPh layers. The ITO electrode preparation and SGraHIL deposition methods were the same as mentioned previously. To prepare the orange stretchable ExciPh, 0.9 mg of orange dopant, $Ir(bt)_2acac$, was mixed with 5 mg of TCTA and 5 mg of TPBi and then dissolved in 1 ml of PU solution. The orange stretchable ExciPh solution was filtered through a 0.45-μm syringe PVDF filter and spin-coated on the SGraHIL at 6,000 rpm for 60 s. The resultant film was then heat-treated at 90 °C for 5 min. Subsequently, the green stretchable ExciPh deposited on the OTMS-treated wafer was transferred onto the PDMS stamp and tensile stress was applied to achieve the desired strain. To strengthen electrical contact and adhesion at the interface, the specimen was heat-treated at 80 °C for 3 min and then brought into contact with the orange stretchable ExciPh. The remaining processes for TPBi, LiF and Al deposition were the same as those used in fabrication by spin-coating.

Full-colour, fully stretchable OLEDs using a transfer-printing method

Four stretchable ExciPh layers were prepared before the device fabrication: $Ir(piq)_3$ for red, $Ir(ppy)_2acac$ for green, FIrPic for blue and $Ir(bt)_2acac$ for orange. The SGraHIL solution was first filtered through a 0.45-μm syringe PVDF filter, spin-coated onto the A-MCSE at 4,000 rpm for 60 s and then the film was annealed at 100 °C for 30 min. Following SGraHIL deposition, the substrate was transferred into a N_2 environment in a glovebox. The OTMS-treated wafers were coated separately with four different stretchable ExciPh layers and dried at 120 °C for 5 min. The PDMS stamp, with a thickness of 2 mm, was gently pressed onto the stretchable ExciPh layer and then released from the wafer. Four stretchable ExciPh layers were sequentially transferred onto the MCSE electrode. Then to establish an electrical interface between the stretchable ExciPh and the C-MCSE, the C-MCSE was gently placed onto the stretchable ExciPh layer and pressed with tweezers to expel any trapped air bubbles. The laminated structure was then annealed at 50 °C for 15 min to guarantee a robust electrical contact.

Characterizations

The optical transmittance (T) of the MCSE was assessed using a UV–Vis spectrophotometer (Lambda 465, PerkinElmer). The sheet resistance was determined using a four-point probe method on a source meter (Keithley 2400, Tektronix). The morphology of the electrodes and organic films was measured using an atomic force microscope (NX10, Park Systems). The surface chemistry of the MCSE was analysed using a Raman spectroscope (LabRAM HR Evolution, HORIBA), equipped with a 532-nm laser. The crystal structure of MXene was observed using an X-ray diffractometer (D8 Advance, Bruker). Surface potential measurements were conducted with a Kelvin probe from KP Technology.

For hydration stability tests, the electrical contacts of the MCSE were shielded using copper tape to prevent the spin-coated film from affecting the contact resistance. The current–voltage curves were measured using a source meter (Keithley 2400, Tektronix) in scans from −2 to 2 V in 0.1-V increments before and after the DIW coating. The hydrogen bonding between AgNW and MXene was quantified using a Fourier-transform infrared spectroscope (Bruker Tensor 27). The carrier mobility of electrodes was assessed using a Hall-effect analyser (HMS-5000, Ecopia). For temperature-dependent resistance measurement, the electrode was wired into a four-point probe geometry using silver paint. The conductivity was recorded from 300 to 10 K in a vacuum environment (<5 torr).

To conduct in situ UV–Vis measurements, three-electrode in situ cells were assembled as follows: $Ti_3C_2T_x$ MXene and MXene/AgNWs were separately spin-coated on 15-mm × 15-mm glass substrates and used as working electrodes. A silver wire was used as the reference electrode. The counter electrodes were overcapacitive films of $Ti_3C_2T_x$ (thickness about 200 nm). To facilitate the passage of the UV–Vis beam through the working electrode and eliminate optical interference from the counter electrode, a circular area (approximately 5 mm in diameter) was excised from the centre of the counter electrode. Walls on the four edges of both working and counter electrodes were fabricated using thick 3M double-sided tape (3M VHB Tape 4910) to create an electrolyte reservoir attached to the electrodes. Electrical contacts between the electrodes and the potentiostat were established using 2-mm graphite foil (0.13 mm thick, Alfa Aesar). The electrolytes used included 1 M sulfuric acid (H_2SO_4, Fisher Scientific, 98%). During the measurements, the in situ UV–Vis cell was secured at the centre of the sample holder, allowing light to pass through the aperture in the cell. Absorption

spectra were recorded over a range from 300 to 1,000 nm with 1-nm intervals using a Thermo Fisher Scientific UV–Vis spectrometer Evolution 201, equipped with a tungsten lamp and a dual-silicon-photodiode detector. The in situ UV–Vis spectra were obtained through synchronous measurements conducted with a Biologic SP-150 potentiostat (BioLogic). The in situ UV–Vis cell was placed on the spectrophotometer holder so that the hole in the counter electrode was aligned with the beam path. Before the in situ tests, the cells underwent precycling through cyclic voltammetry at a scan rate of 20 mV s^{-1} to establish the stable potential window for cells with different working electrodes. The potential windows were determined to be 0.2 to −0.6 V for MXene and 0.2 to −0.4 V for MXene/AgNWs. UV–Vis absorbance spectra of the two electrochemical systems were recorded in situ at every 100 mV increment from 0.2 V to the cathodic limit potential, after allowing the systems to equilibrate at each potential step (about 30 s). In this in situ measurement method, the extended step time (210 s) ensures that the response current reaches zero before proceeding to the next voltage step. In this in situ measurement method, the long step time enables the response current to level off to zero before moving to the next voltage step.

Static stretching tests on the MCSE were conducted by fixing the electrode to a custom-made stretching machine. The contact was secured to the rigid part of the apparatus to maintain consistent contact resistance. Eutectic gallium indium was applied to the contact region, complemented by copper tape as a contact pad. Linear resistance between the copper contact pads was measured using a digital multimeter (Keithley 6500, Tektronix). A specimen, initially 10 mm long, was stretched to 100% at a rate of 10 mm min^{-1}. For cyclic stretching tests, the specimen underwent 500 cycles of stretching from 0 to 40% strain at 100 mm min^{-1}, with resistance measured in real time.

The depth profiles of atomic composition for SGraHIL and SHIL were determined using X-ray photoelectron spectroscopy with a scanning source of monochromatic Al Kα radiation (1,486.6 eV) and Ar sputtering for etching. Concurrently, a UV photoelectron spectroscope (AXIS Ultra DLD, Kratos) assessed the film's WF at specific sputter etching intervals. The UV photoelectron spectroscope was equipped with a helium gas-discharge lamp (excitation energy of 21.2 eV and energy resolution of 200 meV) and a sampling area of 100 μm in diameter and used a 15-V sample bias to reduce accumulation of static charge. The concentration gradient of PFSA in the SGraHIL was measured using a time-of-flight secondary ion mass spectrometry with a 30-keV Bi^+ ion beam and base pressure $<3.8 \times 10^{-9}$ torr.

Steady-state PL spectra and photostability of the thin-film samples were measured using a spectrofluorometer (FP-8500, JASCO) without glass lid encapsulation; the excitation wavelength was 405 nm. The excitation was provided by a 150-W xenon arc lamp. The PLQYs of the stretchable ExciPh under different strain conditions were measured using a Photomultiplier Tube and a monochromator (Acton Research Corporation). The excitation source for these measurements was a 325-nm He:Cd continuous-wave laser (Kimmon Koha). To avoid the effects of absorption by impurities, the stretched specimen was mounted on a quartz substrate. The specimen was then placed in an integration sphere with N_2 flow to minimize oxygen quenching. The PLQY was calculated using several direct and indirect light-emission measurements from the stretched specimen.

The fluorescence recovery after photobleaching analysis was performed using a confocal laser scanning microscope (LSM 900, ZEISS). All samples were encapsulated with a UV-curable epoxy resin to prevent oxygen quenching and subsequently placed in a live-cell chamber. Photobleaching was carried out by irradiating a circular region with a radius of 4.32 μm, using a 410-nm laser. Fluorescence recovery was then monitored at 37 °C, under excitation with the same laser.

TRPL measurements were performed using a picosecond-pulse laser (LDH-P-C-405B, PicoQuant), emitting at 405 nm with a pulse width of <70 ps and a repetition rate of 5 MHz, powered by a PLD 800-B driver. The emitted light from the samples was detected using a PMA Hybrid 07 photon-counting detector and a PicoQuant PicoHarp time-correlated single-photon counting module, which included a microchannel plate photomultiplier tube (R3809U-59, Hamamatsu Photonics). Temperature-dependent TRPL and steady-state PL spectra were acquired using a streak camera system (C10910-01, Hamamatsu Photonics) coupled with the third harmonic (355 nm) of a Nd:YAG laser (PL2250, EKSPLA). Laser output intensity was adjusted according to the measurement timescale: 3% for 200 ns, 5% for 1 μs and 10 μs and 20% for 5 ns.

The Fourier imaging microscopy (FIM) system consists of two main parts: (1) an inverted fluorescence microscope for sample illumination and light collection comprising a 405-nm diode laser and an Olympus IX81 inverted microscope and (2) an optical relay system designed for spectral and polarization analysis. The latter includes a relay lens (Thorlabs), optical filters, a linear polarizer and a spectrometer equipped with a 1,024 × 1,024 CCD array (Princeton Instruments). The sample was optically pumped with a 405-nm diode laser and its PL was collected by means of an oil immersion objective lens (×100, NA = 1.40, Olympus). The collected emission was relayed by means of a $f = 300$ mm lens, which projects the back focal plane of the objective onto the CCD, thereby forming the Fourier plane. A 450-nm long-pass filter removes the redundant light, such as the reflected laser beam, from reaching the CCD. To separate the polarization modes, a linear polarizer was used to decompose the emitted light into two orthogonal p-polarized (pPP) and s-polarized (sPP) components, which were subsequently analysed using a spectrometer. The k-space fitting of the pPP mode was performed within the restricted range $-1.1 < k_x/k_0 < 1.1$ to mitigate the effect of imaging artefacts in the high-k region of the objective lens.

For spectrally resolved FIM, a diffraction grating (300 grooves per mm) was integrated within the optical path of the spectrometer, dispersing the emitted light across the CCD sensor. This enables spectral mapping over a wavelength range of 80 nm, covering the region from $\lambda = 0$ to 1,500 nm. The fine spectral resolution of 0.05 nm allows for detailed Fourier-plane imaging, facilitating high-precision data acquisition over the relevant wavelength range.

Ellipsometry measurements of the light-emitting materials were performed using a variable-angle spectroscopic ellipsometer (J.A. Woollam Co.) across a wavelength range of 200–1,650 nm and detection angles from 45° to 75° in 5° increments. The contact angles were measured using a contact-angle analyser (Femtofab, SmartDrop) at room temperature using DIW and diiodomethane.

Magneto-PL measurements were conducted by recording the PL intensity as a function of the magnetic field using a 405-nm laser as the light source. Grazing-incidence X-ray diffraction was performed with a wavelength of 1.305 Å at beamline 3C of the Pohang Accelerator Laboratory, Republic of Korea. The incident angle on a sample was fixed at 0.15° and Eiger 4M was used to detect the scattered X-ray beam. The PLS-II 3C SAXS beamline data plot program with MATLAB (version 0.1) was used and the data were analysed by Zenodo.

The measurement of the Young's modulus E of the stretchable ExciPh layer began with the application of the stretchable ExciPh solution onto an OTMS-treated SiO_2 substrate, by spin-coating at 2,000 rpm for 60 s, followed by annealing at 90 °C for 5 min. In the next step, a pre-stretched PU substrate is put into conformal contact with the stretchable ExciPh layer. Release of stretching caused buckling of the PU substrate's surface; the E of the stretchable ExciPh was deduced from the wavelength of this buckling pattern as[5]

$$E = 3E_s\left(\frac{1-\upsilon_f^2}{1-\upsilon_s^2}\right)\left(\frac{\lambda}{2\pi d_f}\right), \quad (1)$$

in which E_s is the Young's modulus of the substrate, υ_f and υ_s are the Poisson's ratios of the stretchable ExciPh layer and the substrate, respectively, λ is the wavelength and d_f is the thickness of the stretchable ExciPh.

E quantifies the stiffness of a material and deformation response under stress, whereas hardness measures resistance to local stress (indentation). *E* and indentation hardness are proportionally related regardless of composition, so *E* was also calculated from the hardness as estimated from nanoindentation results obtained using an atomic force microscope (NX10, Park Systems). The force–separation curve obtained from the indentation was analysed using the Oliver–Pharr model to calculate hardness.

Rigid OLEDs that had glass lid encapsulations were characterized using a source meter (Keithley 236, Tektronix) and a spectroradiometer (CS-2000, Minolta). The fully stretchable OLEDs were characterized in a N_2-filled glovebox: time-resolved electroluminescence spectra of the fully stretchable OLEDs were captured using a streak camera (Hamamatsu Photonics), with voltage pulses applied to the device for durations of 5 ms. The radiometric properties of the fully stretchable OLEDs were assessed using a goniometer set-up, with calibrated photodetectors and a spectrometer mounted on a rotating arm perpendicular to the device.

MD simulation

All-atom MD simulations were used for a model system of fully stretchable OLED material, based on a mixture with the experimental composition: 9.1 wt% $Ir(ppy)_2acac$, 37.9 wt% TCTA, 37.85 wt% TPBi and 15.2 wt% PU. The initial configurations of the mixture were prepared using the Monte Carlo method, in which the constituents were randomly positioned within a simulation box using periodic boundary conditions and an initial total density of 0.25 g cm^{-3}, all while accounting for their excluded volumes. The simulation box contained 25 $Ir(ppy)_2acac$ molecules, 84 TCTA molecules, 95 TPBi molecules and four PU molecules, with the PU having a degree of polymerization of 20. With this initial configuration, isothermal–isobaric MD simulations for the mixture were then performed using the Forcite module with the universal force field, incorporating partial atomic charges derived using the electrostatic potential method. The method involved fitting the electrostatic potential surface of the optimized structures of constituents, in which geometry optimizations of each constituent species were carried out by density functional theory at the B3LYP functional level with a DNP basis set, using DMOL3 as implemented in the Materials Studio package. For the MD simulation of the unstretched system, the Nosé–Hoover–Langevin thermostat and the Berendsen barostat were used to maintain the temperature at 298 K and the pressure at 1 bar, respectively. The unstretched MD systems were equilibrated over 100 ns using a 1-fs time step. Subsequently, the stretched state at a specified strain was simulated using the Souza–Martin method, applying an elongational force along the *z* direction with external stress settings of $\tau_{zz} > 0$ and $\tau_{xx} = \tau_{yy} = -1$ bar, while all other stress components were kept at zero. Stretching was performed by setting τ_{zz} to 0.15 GPa and continued until the desired strain was reached, followed by geometry optimization for each stretched sample at the specified strain. For all MD runs, the electrostatic potential energy was calculated by the particle–particle particle–mesh method with an accuracy of 0.001 kcal mol^{-1} and buffer width 2 Å and the van der Waals potential energy was calculated by the atom-based technique with a cut-off distance of 12.5 Å and a spline width of 1 Å.

Data availability

All of the data supporting this manuscript are available in the form of Source Data files and the supplementary material. Source data are provided with this paper.

Acknowledgements This research was supported by a National Research Foundation of Korea grant, financed by the Korean government's Ministry of Science, ICT & Future Planning (RS-2025-00560490) and the Pioneer Research Center Program through the National Research Foundation of Korea, financed by the Ministry of Science, ICT & Future Planning (RS-2022-NR067540). This work was also supported by the Nano & Material Technology Development Program through the National Research Foundation of Korea financed by the Ministry of Science and ICT (RS-2024-00416938). D.Z., T.Z. and Y.G. acknowledge support for MXene synthesis and chemical modification from US National Science Foundation grants DMR-2041050 and CHE-2318105 (M-STAR CCI).

Author contributions H.Z. and T.-W.L. conceived the overall concept. T.-W.L. supervised the project. H.Z., H.-W.K. and S.J.H. initiated the proof-of-concept experiments of fully stretchable OLED devices. H.Z. and H.-W.K. designed and optimized the fully stretchable OLEDs and fabricated devices for analysis and demonstrations. H.Z. and H.-W.K. conducted most of the data analysis and interpretation. D.Z. and T.Z. synthesized MXene and prepared its colloidal solutions, D.Z. performed in situ UV–Vis absorption spectroscopy and T.Z. conducted temperature-dependent resistance measurements under the supervision of Y.G. W.J.J. fabricated the rigid OLEDs. B.H. conceived the magneto-PL experiments and H.Y. performed the corresponding measurements. Y.T. conducted temperature-dependent streak camera measurements under the guidance of C.A. J.H. performed MD simulations. S.C. carried out FIM and spectrally resolved FIM measurements and analysis under the supervision of J.C.K. J.S.K. contributed to transient electroluminescence measurements. D.-H.K. assisted with PLQY and ellipsometry data acquisition. H.J.Y. performed in situ UV photoelectron spectroscopy and X-ray photoelectron spectroscopy measurements. J.P. and E.Y. carried out TRPL data acquisition and K.Y.J. conducted further streak camera measurement. A.K.H. synthesized Crown-CPE under the supervision of H.Y.W. M.-J.S., Y.A. and H. Yang performed grazing incidence X-ray diffraction measurements. H.C. and Q.Z. assisted with UV–Vis and PL measurements. C.-Y.P. performed contact-angle measurements. K.-N.K. contributed to the design of the stretching jig. L.A. synthesized 2PTPS under the guidance of Y.-H.K. H.Z. visualized the data and drafted the initial manuscript and other related documents. T.-W.L. provided substantial revisions. H.-W.K., D.Z. and Y.G. reviewed and edited the manuscript.

Competing interests The authors declare no competing interests.

Additional information
Supplementary information The online version contains supplementary material available at https://doi.org/10.1038/s41586-025-09904-0.
Correspondence and requests for materials should be addressed to Yury Gogotsi or Tae-Woo Lee.
Peer review information *Nature* thanks Paloma dos Santos and the other, anonymous, reviewer(s) for their contribution to the peer review of this work.

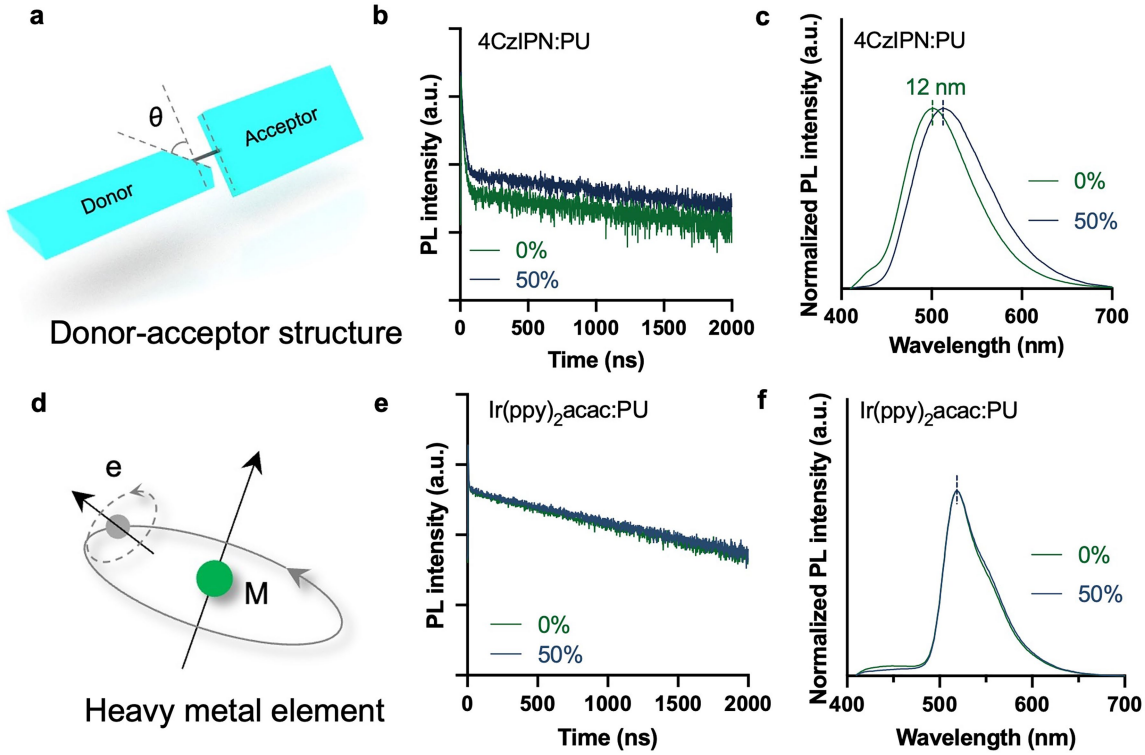

Extended Data Fig. 1 | Photophysics of TADF and phosphorescence under stretching. a, Schematic illustration of the donor–acceptor structure in the small-molecule TADF molecules. **b**,**c**, TRPL and PL spectra of 4CzIPN at a concentration of 1.5 mg ml^{-1} in a 2 mg ml^{-1} PU matrix, both before and after application of 50% tensile strain. **d**, Schematic illustration of SOC facilitated by the heavy-metal atom in the phosphorescent materials. **e**,**f**, TRPL and PL spectra of Ir(ppy)$_2$acac at a concentration of 1.5 mg ml^{-1} in a 2 mg ml^{-1} PU matrix, measured before and after application of 50% tensile strain.

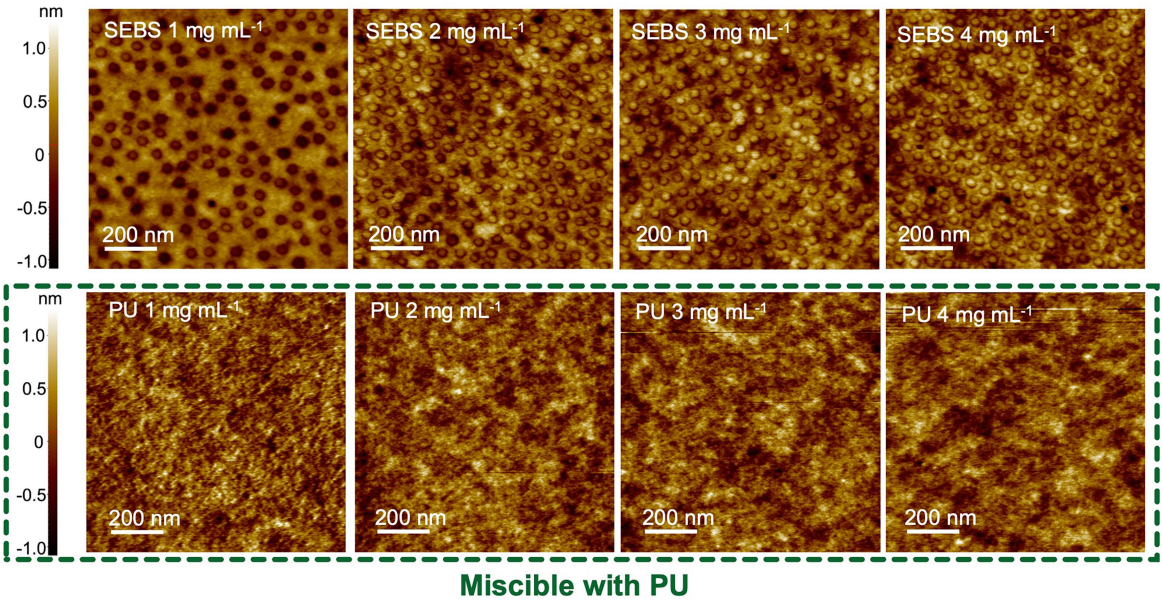

Extended Data Fig. 2 | Effect of elastomer content on the morphology of the stretchable ExciPh layer. Atomic force microscopy of ExciPh, with varying loadings of SEBS (top images) and PU (bottom images).

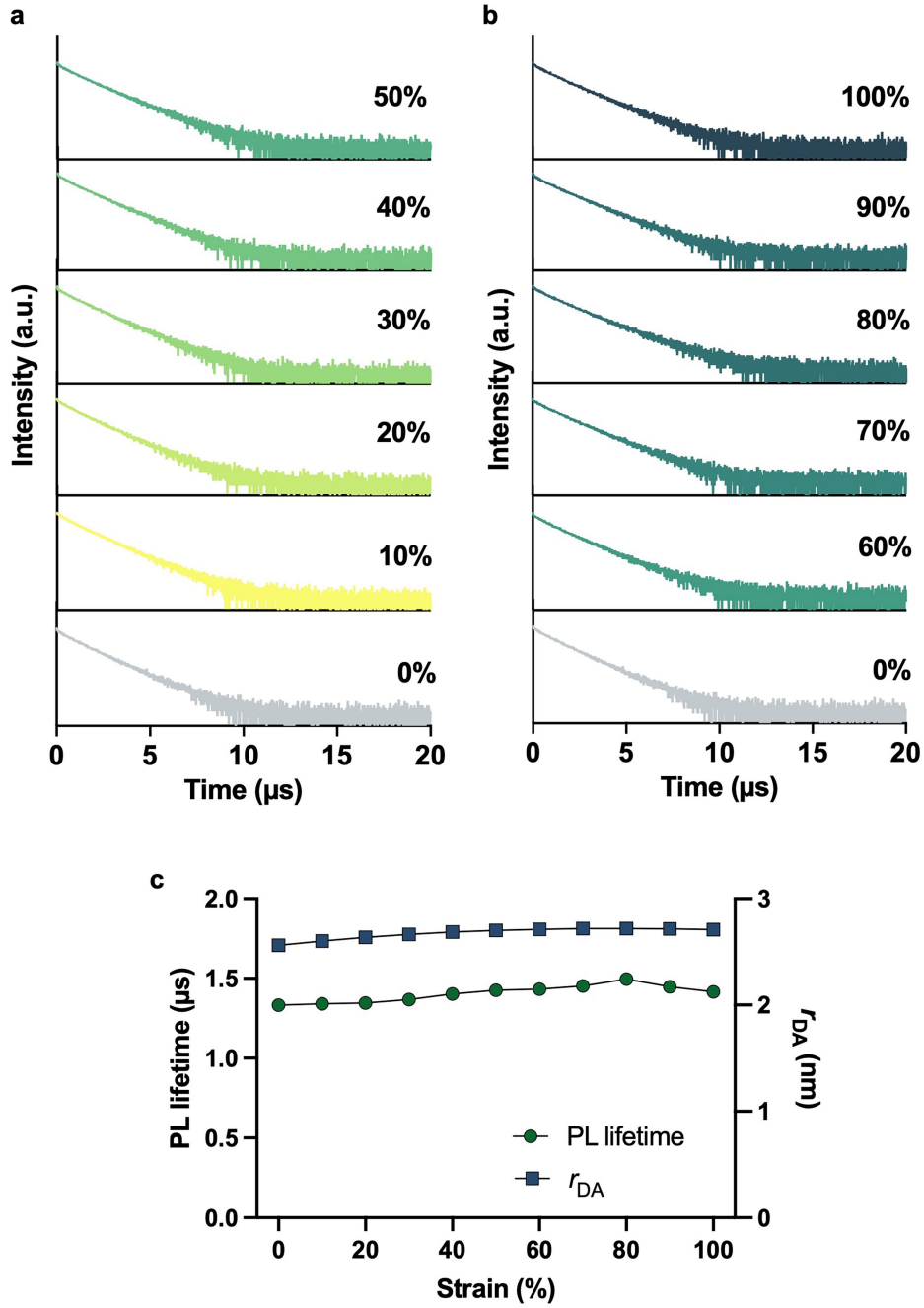

Extended Data Fig. 3 | Effect of mechanical stretching on the exciplex energy transfer. a,**b**, TRPL spectra of ExciPh films under increasing tensile strain (0–100%). ExciPh layers were transferred onto quartz substrates, strained and encapsulated with a glass lid to prevent oxygen quenching. **c**, Corresponding PL lifetimes and estimated donor–acceptor distance (r_{DA}) in terms of tensile strain (see details in Supplementary Text 6 for r_{DA} calculation).

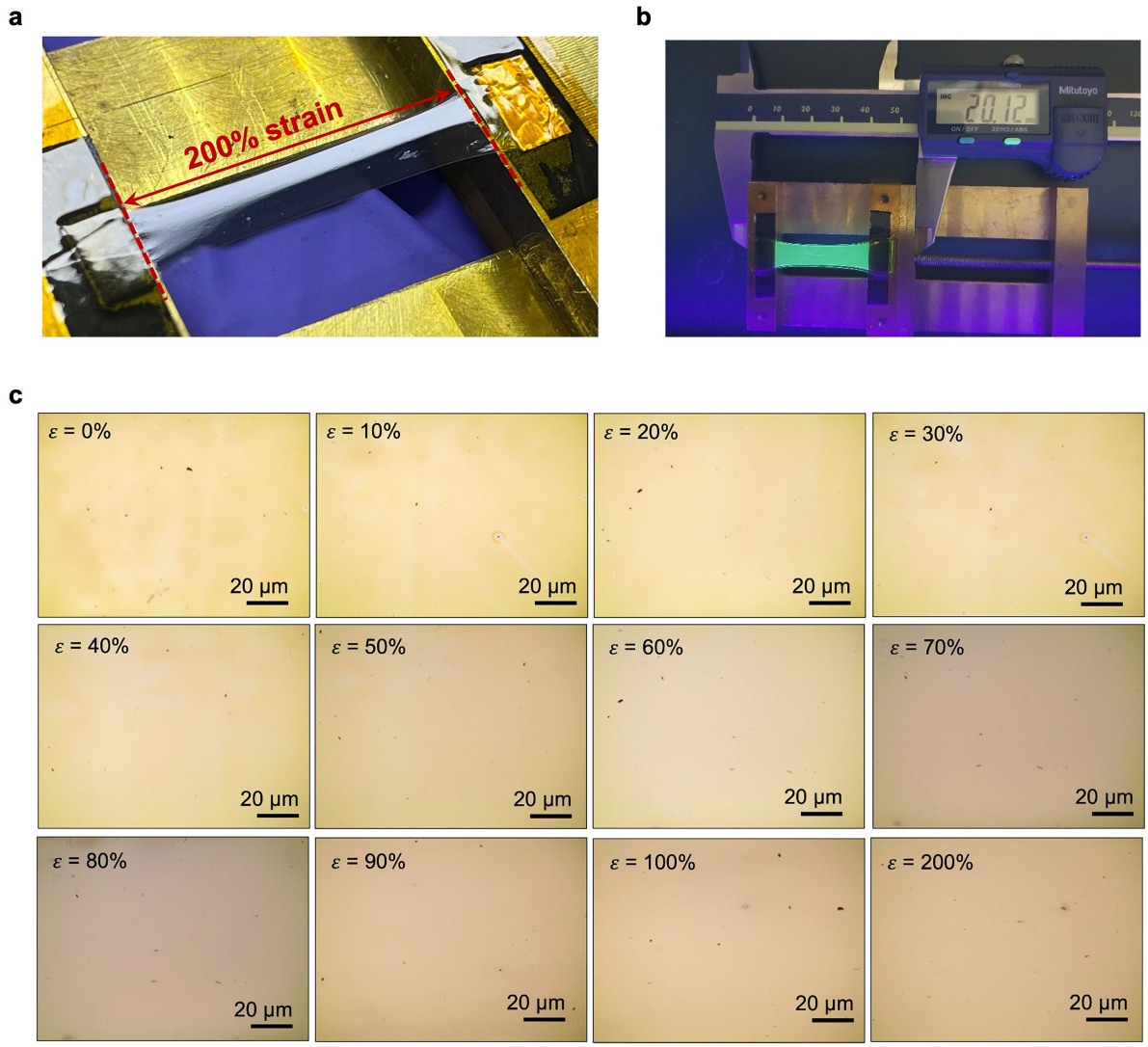

Extended Data Fig. 4 | Mechanical stretchability of the stretchable ExciPh layer. a, Digital photograph of SGraHIL/ExciPh on the substrate applied with 200% tensile strain. The highly reflective surface of the stretchable ExciPh indicates that no microcracks formed during stretching. **b**, Digital photograph of SGraHIL/ExciPh under 200% strain under UV irradiation. Initial length was 10 mm. **c**, Optical microscopic images of in situ stretching test on SGraHIL/ExciPh without using an encapsulation layer on top.

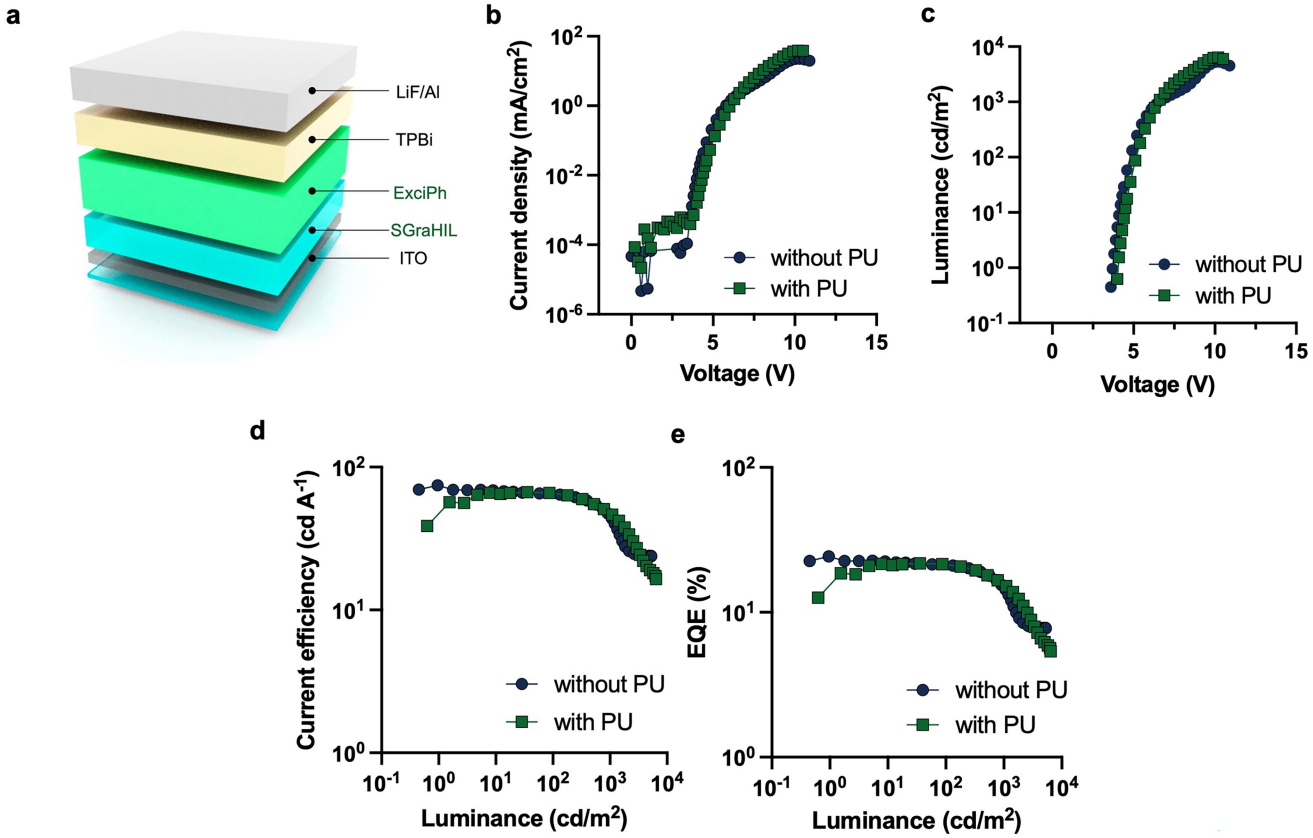

Extended Data Fig. 5 | Characteristics of OLEDs using a stretchable ExciPh layer. a, Schematic of the high-efficiency OLED that uses SGraHIL and ExciPh. Device structure: ITO (70 nm)/SGraHIL (82 nm)/ExciPh with or without PU (50 nm)/TPBi (45 nm)/LiF (2 nm)/Al (100 nm). **b**–**e**, Electroluminescent characteristics of this OLED.

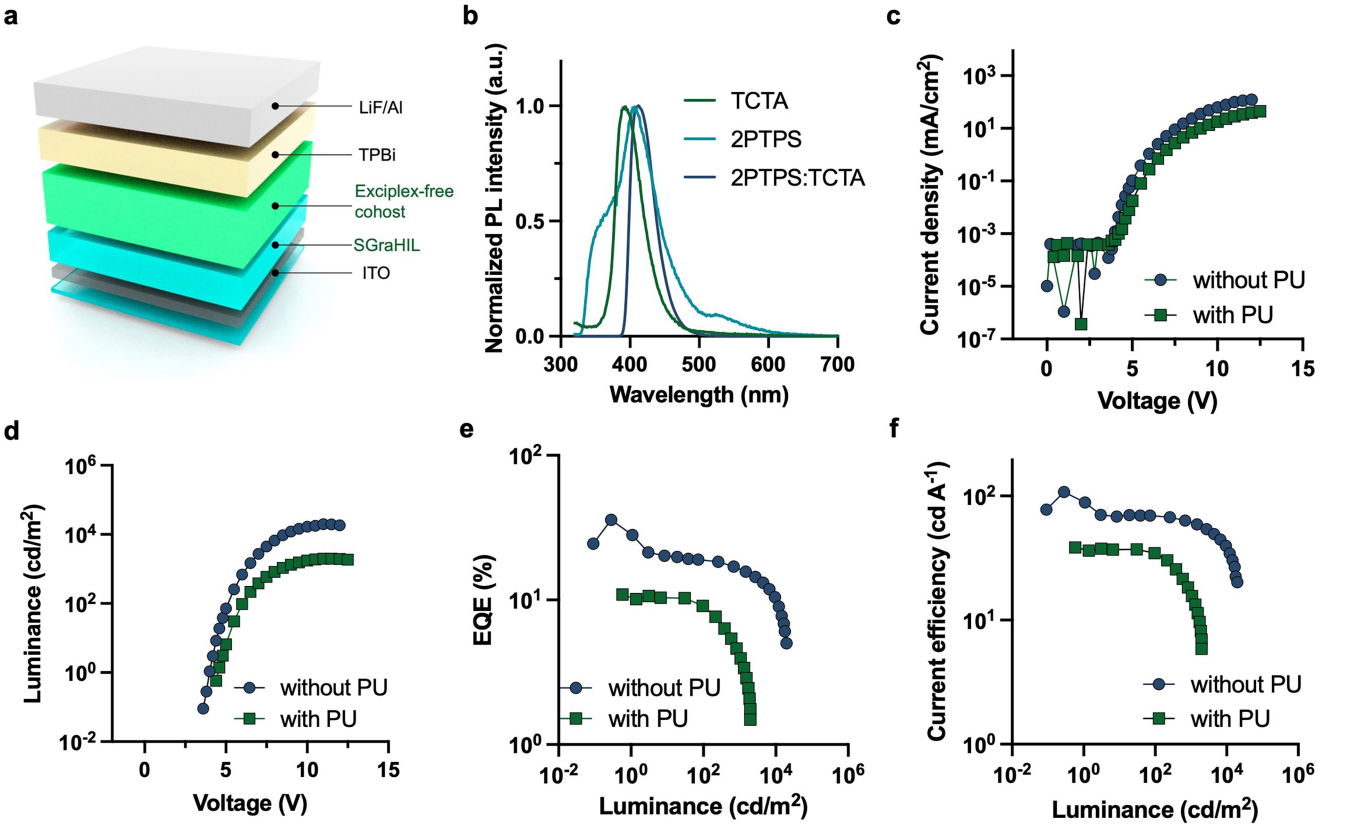

Extended Data Fig. 6 | Electroluminescent performance of phosphorescent OLEDs using exciplex-free cohosts. a, Device schematic of phosphorescent OLEDs comprising exciplex-free cohosts of Ir(ppy)$_2$acac:TCTA:2PTPS (0.9:5:5 w/w/w). Device structure: ITO (70 nm)/SGraHIL (82 nm)/Ir(ppy)$_2$acac:exciplex-free cohosts with or without PU (50 nm)/TPBi (45 nm)/LiF (2 nm)/Al (100 nm). **b**, PL spectra of TCTA, 2PTPS and the 2PTPS:TCTA blend, confirming the absence of exciplex formation. **c**–**f**, Electroluminescent characteristics of the OLEDs based on exciplex-free cohost systems.

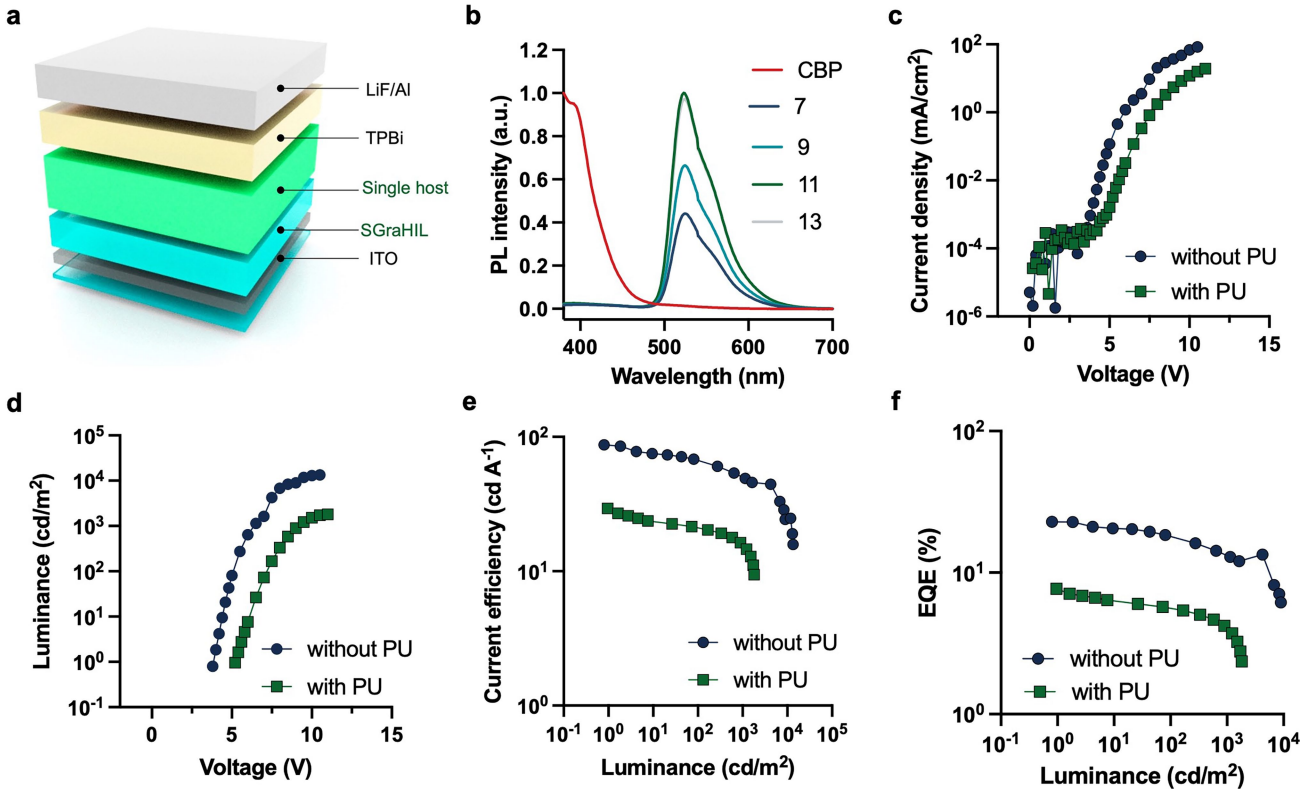

Extended Data Fig. 7 | Characteristics of phosphorescent OLEDs using a single host. a, Device schematic of phosphorescent OLEDs comprising a single host of $Ir(ppy)_2acac$:CPB (0.9:10 w/w). Device structure: ITO (70 nm)/SGraHIL (82 nm)/$Ir(ppy)_2acac$:single host with or without PU (50 nm)/TPBi (45 nm)/LiF (2 nm)/Al (100 nm). **b**, PL spectra of pristine CBP and 0.9 mg ml^{-1} $Ir(ppy)_2acac$ blended with varying CBP concentrations. **c**–**f**, Electroluminescent characteristics of the OLEDs based on exciplex-free cohost systems.

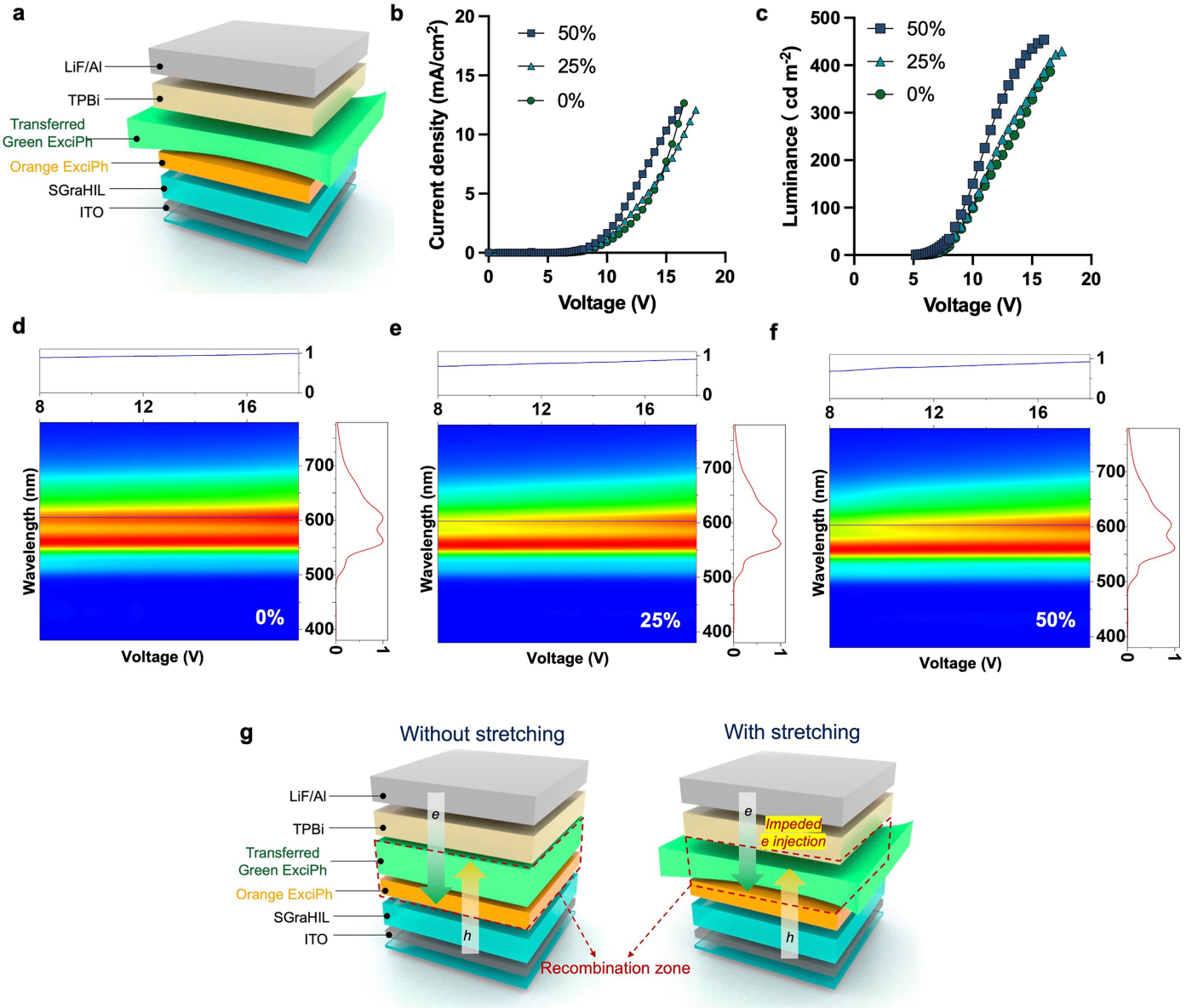

Extended Data Fig. 8 | Effect of mechanical stretching of the stretchable ExciPh layer on charge-carrier recombination in OLEDs. a, Schematic of OLED devices that use orange and green ExciPh layers. The orange ExciPh layer was deposited directly on the SGraHIL layer. The green ExciPh was deposited on an OTMS-treated wafer and transferred onto a PDMS stamp. Then the green ExciPh on the stamp was delicately pressed onto the orange ExciPh while retaining tensile strain. **b**,**c**, Current density–voltage and luminance–voltage curves of OLEDs with green ExciPh under different tensile strains. **d**–**f**, Evolution of electroluminescent spectrum with 0%, 25% and 50% tensile strain applied to the green ExciPh. Horizontal profiles on the top represent the evolution of electroluminescent intensity at 603 nm, which corresponds to the peak position of orange ExciPh. Vertical profiles on the right-hand *y* axes: electroluminescent spectrum at 18 V. **g**, Schematic of recombination zone shift to the green ExciPh region owing to impeded electron injection under stretching. Green ExciPh: stretchable exciplex-assisted phosphorescent layer using $Ir(ppy)_2acac$ as the dopant. Orange ExciPh: stretchable exciplex-assisted phosphorescent layer using $Ir(bt)_2acac$ as the dopant.

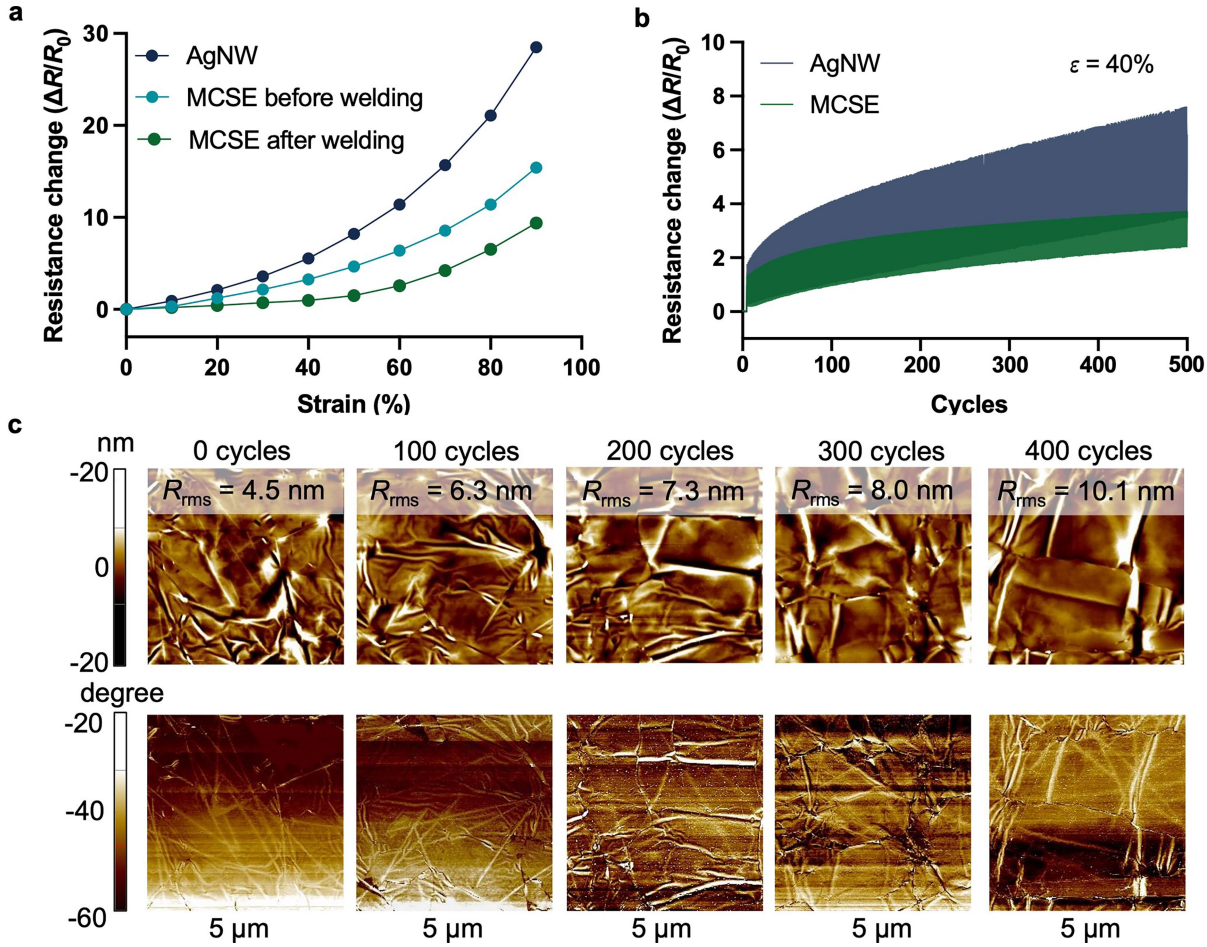

Extended Data Fig. 9 | Characterization of the mechanical stability of MCSEs. a,**b**, Static stretching tests (ε = 100%) and cyclic stretching tests (ε = 40%) of the AgNW stretchable electrode and MCSEs before and after welding. **c**, Atomic force microscopy topography of MCSE before, during and after tensile strain (ε = 40%).

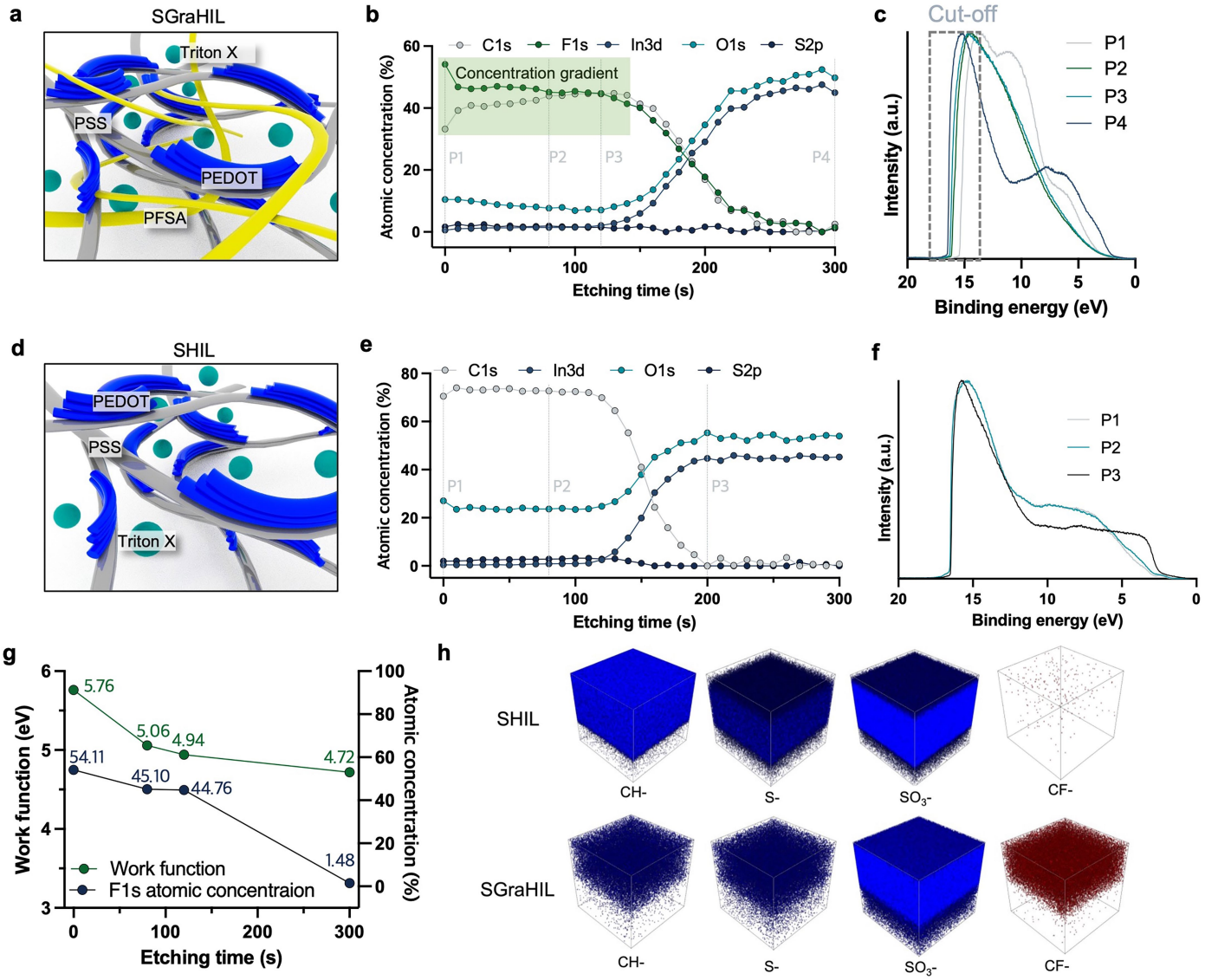

Extended Data Fig. 10 | Origin of WF gradient in SGraHIL. a, Schematic illustration of SGraHIL. **b**, X-ray photoelectron spectroscopy depth profile of SGraHIL. P1 to P4 represent four positions with 0, 80, 120 and 200 s of sputter etching time, respectively. **c**, UV photoelectron spectroscopy measurement of SGraHIL at positions P1, P2, P3 and P4. **d**, Schematic illustration of conventional SHIL. **e**, UV photoelectron spectroscopy measurement of positions P1, P2 and P3. **f**, UV photoelectron spectroscopy measurement of SHIL at positions P1, P2 and P3. **g**, Correlation of WF and F1s atomic concentration profiles in terms of etching time (data extracted from **b** and **c**). **h**, Time-of-flight secondary ion mass spectrometry 3D mapping for $[CH]^-$, $[S]^-$, $[SO_3]^-$ and $[CF]^-$ ions in SHIL and SGraHIL. SHIL, stretchable hole injection layer composed of PEDOT:PSS AI 4083 and Triton X-100; SGraHIL, stretchable gradient hole injection layer composed of PEDOT:PSS, PFSA and Triton X-100.